Monthly Notices of the ROYAL ASTRONOMICAL SOCIETY

MNRAS **552,** 1–28 (2026)
Advance Access publication 2026 September 24

https://doi.org/10.1093/mnras/stag1806

A VLBA survey of radio stars in the Orion Nebula Cluster – III. Inter-epoch variability analysis

Eoin T. O'Kelly [1]*, Jan Forbrich [1,2], Sergio A. Dzib [3] and Jaime Vargas-González [4]

[1]*Centre for Astrophysics Research, University of Hertfordshire, College Lane, Hatfield AL10 9AB, UK*
[2]*European Space Agency (ESA), European Space Research and Technology Centre (ESTEC), Keplerlaan 1, Noordwijk, NL-2201 AZ, the Netherlands*
[3]*Max-Planck-Institut für Radioastronomie, Auf dem Hügel 69, D-53121 Bonn, Germany*
[4]*Joint ALMA Observatory, Alonso de Córdova 3107, Vitacura, Santiago, Chile*

Accepted 2026 September 13. Received 2026 September 10; in original form 2026 July 13

ABSTRACT

We present a multi-epoch Very Long Baseline Array (VLBA) survey of radio sources in the Orion Nebula Cluster, updating the detection statistics and investigating inter-epoch variability. The data set comprises eight C-band (4–8 GHz) epochs targeting 575 radio sources previously identified in deep Very Large Array surveys. VLBA observations result in resolutions of milliarcseconds and are only sensitive to high brightness temperatures, meaning only non-thermal emission is observed. We detect 226 unique radio sources corresponding to a detection fraction of 39 per cent. The majority of sources (∼83 per cent) are detected only once, indicating that non-thermal emission associated with young stellar objects (YSOs) is highly intermittent. To quantify variability, we use per-epoch peak flux densities and the variability factor defined as the ratio between the maximum and minimum fluxes. We identify 21 sources (∼9 per cent of detected sources) that exhibit high variability defined as a change of flux density by at least a factor of 5. We crossmatch with the COUP *Chandra* survey to identify sources as YSOs. We identify COUP counterparts for ∼56 per cent of the detected sources. The remaining population cannot be explained solely by variability or background contamination, suggesting a population of radio-detected YSOs without X-ray counterparts. We find a clear correlation between radio and X-ray luminosities consistent with the Güdel–Benz relation, the empirical relation between non-thermal radio and thermal X-ray emission for magnetically active stars.

Key words: radiation mechanisms: non-thermal – instrumentation: high angular resolution – stars: formation – stars: variables: T Tauri, Herbig Ae/Be – radio continuum: stars.

1 INTRODUCTION

Star formation is associated with high-energy processes and young stellar objects (YSOs) are known to be energetic radio sources (G. A. Dulk 1985; E. D. Feigelson & T. Montmerle 1999). Centimetric radio emission from YSOs can be either thermal free–free produced by ionized material or non-thermal (gyro)synchrotron generated by (mildly) relativistic electrons gyrating in magnetic fields associated with coronal-type activity (e.g. M. Güdel 2002).

High-energy events irradiating circumstellar discs may play an important role in disc evolution, chemistry and planet formation (e.g. E. D. Feigelson, G. P. Garmire & S. H. Pravdo 2002; B. Zhao et al. 2020). For example, E. D. Feigelson (2010) argues that high-energy irradiation may be critical in establishing disc turbulence via ionization and enabling magneto-rotational instability, alongside other mechanisms such as hydrodynamical or gravitational instabilities.

Disentangling thermal free–free and non-thermal gyrosynchrotron emission can be challenging, with an interest in non-thermal emission as it traces high-energy processes associated with magnetic activity within the coronae of YSOs (e.g. E. D. Feigelson & T. Montmerle 1999; J. Vargas-González 2024). The primary diagnostics used to distinguish between emission types are: polarization (with gyrosynchrotron being circularly polarized and synchrotron linearly polarized), spectral index, variability and brightness temperature.

The spectral index, defined as α in $S_\nu \propto \nu^\alpha$, can provide insight into the emission mechanism where positive spectral indices are generally associated with thermal emission and negative indices with non-thermal emission (e.g. G. B. Rybicki & A. P. Lightman 1986; T. L. Wilson, K. Rohlfs & S. Hüttemeister 2009; A. Scaife 2012). However, interpretation of spectral indices can be ambiguous as there is a turnover within the spectrum and gyrosynchrotron emission can be time variable; these can correspond to different physical regimes (e.g. optical depth; see G. A. Dulk 1985; A. Benz 2002; M. Güdel 2002; R. A. Osten & S. J. Wolk 2009). Importantly, it should be highlighted that the relatively narrow frequency coverage of the observations presented here (see Section 2) means in-band spectral indices would require higher signal-to-noise to reliably measure them (e.g. U. Rau & T. J. Cornwell 2011, discuss that uncertainties of measured spectral indices increase at lower signal-to-noise).

* E-mail: e.okelly@herts.ac.uk

© The Author(s) 2026.
Published by Oxford University Press on behalf of Royal Astronomical Society. This is an Open Access article distributed under the terms of the Creative Commons Attribution License (https://creativecommons.org/licenses/by/4.0/), which permits unrestricted reuse, distribution, and reproduction in any medium, provided the original work is properly cited.

Downloaded from academic.oup.com/mnras/article/552/4/stag1806/8834038 by guest on 23 October 2026

Very Long Baseline Interferometry (VLBI) is sensitive only to emission with high brightness temperatures, which effectively restricts detections to non-thermal processes (e.g. M. Felli & R. Spencer 1989; A. Thompson, J. Moran & G. Swenson 2017). Thermal free–free emission has a maximum brightness temperature $\lesssim 10^5$K (e.g. J. Condon & S. Ransom 2016), whereas non-thermal emission can reach temperatures of several million kelvin (e.g. P. Andre 1996). The minimum detectable brightness temperature can be expressed in terms of the flux density S, observing wavelength λ, and baseline length D, where $S = 2kT_B\Omega/\lambda^2$ and the source solid angle is $\Omega \simeq \pi(\lambda/2D)^2$, giving the minimum detectable brightness temperature,

$$(T_B)_{\mathbf{min}} \simeq \frac{2}{\pi k} D^2 S_{\rm min}, \tag{1}$$

where k is the Boltzmann constant (A. Thompson et al. 2017). Equation (1) shows that longer baseline length observations are only sensitive to high brightness temperatures.

The Very Long Baseline Array (VLBA) has a maximum baseline of 8611 km resulting in milliarcsecond resolutions. At these resolutions even a relatively faint detection of 0.2 mJy beam^{-1} corresponds to a brightness temperature of $T_B \approx 10^7 K$ (equation 1), well above the maximum expected for thermal emission. Therefore, detections are associated with non-thermal emission. The smallest angular size that can be probed is limited by the synthesized beam size, if a source is unresolved the true angular size must be smaller than the size of the beam; therefore, this corresponds to a lower limit of the brightness temperature (e.g. M. Felli & R. Spencer 1989; P. Andre et al. 1991). Consequently, VLBI is a powerful tool to isolate non-thermal radio emission from YSOs (e.g. S. A. Dzib et al. 2021; J. Forbrich et al. 2021; R. Launhardt et al. 2022; S. A. Dzib et al. 2024).

The Orion Nebula Cluster (ONC) is the nearest region of active high-mass star formation and provides a unique opportunity to observe a large number of sources within a single primary beam. At the observing frequency of this data set the full width at half-maximum (FWHM) of the primary beam is ∼7 arcmin, allowing simultaneous observations of many sources within the cluster. The ONC is relatively nearby, with recent distance estimates ranging from 414 ± 7 pc (K. M. Menten et al. 2007), 403^{+7}_{-6} pc (M. A. Kuhn et al. 2019) to 388 ± 5 pc (M. Kounkel et al. 2017) and the most recent of 388.5 ± 1.7 pc (S. A. Dzib et al. 2026a). When a single distance is required in this work we adopt the value from S. A. Dzib et al. (2026a).

The radio source population of the ONC has been studied extensively with the US National Radio Astronomy Observatory (NRAO) Very Large Array (VLA) since the earliest surveys by G. Garay, J. M. Moran & M. J. Reid (1987) and E. Churchwell et al. (1987), which detected 21 and 22 radio sources, respectively. Subsequent VLA observations by L. A. Zapata et al. (2004a) expanded the radio population and detected 77 sources. A deep VLA survey conducted by J. Forbrich et al. (2016) detected 556 sources. The source positions from this survey form the basis for the majority of the VLBA phase centres used in our work. In addition, 19 sources identified by the VLA survey of J. Vargas-González et al. (2021) were also included resulting in a total of 575 targeted source positions. It is important to note that it is known that not all of these VLA-detected sources are stellar in origin and would not be detected in VLBA observations (e.g. J. Forbrich et al. 2016; J. Vargas-González et al. 2021, both discuss detections of jets and outflows).

Recent upgrades to both the VLA and VLBA have significantly improved sensitivity and observational capabilities. The development of the DiFX software correlator (A. T. Deller et al. 2007, 2011) enables the correlation of many phase centres within a single primary beam required due to the field-of-view limitations inherent to VLBI observations (see Section 3). Earlier VLBI observations were limited to correlating only a small number of phase centres, however the DiFX software correlator allows all radio sources identified in the VLA surveys of the ONC discussed above to be targeted in a single observation with many phase centres.

Given that the VLBA observations presented here are sensitive exclusively to non-thermal radio emission the connection to X-ray studies of the ONC should be considered. An empirical correlation between non-thermal radio and thermal X-ray emission, the Güdel–Benz relation, was first identified by M. Guedel & A. O. Benz (1993) and A. O. Benz & M. Guedel (1994). This correlation has been further studied within the ONC using VLA observations by J. Forbrich & S. J. Wolk (2013) and V. Yanza et al. (2022) whose focus was on M17 (Omega Nebula or NGC 6618) but they also studied this within the ONC.

For the X-ray perspective required here we use the *Chandra* Orion Ultradeep Project (COUP), which provides a comprehensive X-ray census of the ONC based on observations with NASA's *Chandra* X-ray Observatory (K. V. Getman et al. 2005). This was also done for the other studies mentioned previously that used this X-ray census similarly. The COUP data set consists of six nearly consecutive exposures spanning 13.2 d, a total exposure time of 9.7 d and covers an area of approximately 17 × 17 arcmin, which is significantly larger than the VLBA primary beam. The resulting catalogue contains over 1600 X-ray sources and is currently the most sensitive X-ray survey of the ONC. The COUP catalogue allows cross-matching with radio sources to identify them as being associated with the young stellar population, since elevated X-ray emission in this context is associated with magnetically active pre-main sequence stars (e.g. E. D. Feigelson & T. Montmerle 1999). However, the absence of an X-ray counterpart does not preclude it from being a YSO as extinction associated with deeply embedded objects and source variability can be factors (e.g. J. Forbrich et al. 2021). In this work, the COUP catalogue is used to investigate the empirical relationship between non-thermal radio emission and thermal X-ray emission, which is presented in Section 4.6.

In this paper we present updated detection statistics and radio photometry of non-thermal sources within the ONC. This continues the non-thermal census presented in Paper I of this series by J. Forbrich et al. (2021) extending their work and investigating the associated radio variability using per-epoch peak flux densities. An accompanying fourth paper will update the astrometry and proper motions continuing the work in Paper II of this series by S. A. Dzib et al. (2021), and a fifth paper will investigate intra-epoch variability using these new VLBA epochs continuing the work presented by J. Vargas-González (2024).

2 OBSERVATIONS AND DATA REDUCTION

The data set consists of eight epochs of VLBA observations, each approximately 7 h in duration. Observations were in the C-band (4–8 GHz) at a central observing frequency of 7.196 GHz in dual polarization with an aggregate bandwidth of 256 MHz. To minimize the impact of parallax effects on astrometry all observations were scheduled at the same time of the year. The observing setup and data reduction procedures for the first four epochs

Downloaded from academic.oup.com/mnras/article/552/4/stag1806/8834038 by guest on 23 October 2026

Table 1. Details of VLBA observations for all eight epochs.

Number	Epoch	Date, time (UT)	Beam[a]	Antennas	Correlated positions
1	BF117	2015-10-26, 6:25-14:23	4.7 × 1.6	8 (no MK, HN)	556
2	BF123A	2017-10-26, 6:23-14:21	4.4 × 1.3	9 (no SC, PT[b], HN[b])	557
3	BF123B	2017-10-27, 6:19-14:17	4.1 × 1.4	8 (no SC, HN, PT[b])	557
4	BF123C	2018-10-26, 6:24-14:22	2.8 × 1.2	10	557
5	BF131A	2020-10-25, 6:26-14:24	2.7 × 1.1	10	575
6	BF131B	2020-10-29, 6:10-14:08	2.7 × 1.1	10	575
7	BF131C	2021-10-30, 5:37-13:34	3.0 × 1.6	9 (no LA)	575
8	BF131D	2021-10-31, 6:03-14:01	3.4 × 1.3	9 (no LA)	575

Notes. Columns are (left to right): epoch number, epoch name, date and times of observations, beam size, antennas, number of correlated positions.
[a]Synthesized beam size (FWHM) in milliarcseconds.
[b]Operational but flagged during processing.

are described by J. Forbrich et al. (2021). The dates of the four new epochs, identified by their project codes (BF131A, BF131B, BF131C, and BF131D) and numbered sequentially as the fifth through eighth epochs, are listed in Table 1. The fifth and sixth epochs, observed in 2020, are separated by 4 d, while the seventh and eighth epochs, observed in 2021, are separated by 1 d. This epoch spacing enables the investigation of radio variability on these shorter time-scales.

The pointing centre of all eight VLBA observations is RA = $05^{h}35^{m}14.^{s}479$ and Decl.=$-05^{\circ}22'30.''57$ (J2000), and is the same as that used in the VLA observations of J. Forbrich et al. (2016). As the VLBA and VLA have the same primary beam sizes the VLBA observations effectively cover the same region as the earlier VLA survey.

Phase referencing was performed using the nearby calibrator J0541-0541, located 1.6° in angular distance from the ONC, with a time of 40 s on the calibrator and 120 s on the target. The calibrator was correlated at the position RA = $05^{h}41^{m}38.^{s}083384$ and Decl. = $-05^{\circ}41'49.''42839$.[1] This resulted in approximately 4.7 h of on-source integration time per epoch. Variations in antenna availability between epochs result in the differences in (u, v) coverage and synthesized beam size which are listed in Table 1.

The data reduction for the newly acquired epochs was carried out using the standard calibration methodology outlined by J. Forbrich et al. (2021), employing the Astronomical Image Processing System (AIPS) software suite (E. W. Greisen 2003). As part of the calibration process, systematic delays were mitigated by accounting for ionospheric total electron content, derived from contemporaneous GPS data. Additionally, corrections were applied based on the latest Earth orientation parameters from the US Naval Observatory.

To correct for ionospheric delays three blocks of geodetic observations were obtained per epoch, each 30 min in duration. These were observed simultaneously between 4.112 and 7.260 GHz of known calibrator sources from the NRAO calibrator catalogue[2] spaced across the sky. Residual delays stemming from clock instabilities and zenith atmospheric path differences were subsequently determined through geodetic block observations and subtracted, following the approach of M. J. Reid & A. Brunthaler (2004). Further calibration included compensating for electronic delays and discrepancies across the IF bands, using the bright calibrator J0530+1331. Finally, phase solutions from the reference source were interpolated and uniformly applied to all individually correlated science targets.

Fig. 1 illustrates the spatial distribution of all 575 correlated VLA source positions used in this work overlaid on a VISION 2.1 μm image of the ONC. The cyan squares denote the targeted VLBA phase centres and their size corresponds to the initial 4 × 4 arcsec imaging regions. Radio source detections, defined by a signal-to-noise ratio of ≥ 6.5 from `imfit` (see Section 3) are marked by yellow circles. The large white circle indicates the FWHM of the VLBA primary beam.

3 DATA ANALYSIS

The source detections and statistics for the first four epochs are presented by J. Forbrich et al. (2021), and astrometric results are reported by S. A. Dzib et al. (2021). This work extends the analysis to include four additional VLBA epochs from the BF131 project, with a focus on photometry.

All 575 target positions were imaged in each of the four new epochs in Stokes *I*, resulting in 2300 images and a total of 4527 images across all eight epochs. Circular polarization was investigated by producing Stokes *V* images for all detections in each epoch, where a detection has a signal-to-noise ratio of ≥ 6.5 as measured by the CASA task `imfit` (see below for further discussion; CASA Team 2022).

To identify peaks within a wide field we use images of 8192^2 pixels with a pixel size of 0.5 mas and natural weighting. This corresponds to an area per image of approximately 16 square arcsec (corresponding to $\sim 2.6 \times 10^6$ square AU at the distance of the ONC) which is sixteen times larger than the image sizes from J. Forbrich et al. (2021). The images were centred on the VLA source positions identified by J. Forbrich et al. (2016). This large search area was chosen to maximize the chances of detecting systems with multiple components or sources with significant positional offsets. Although most detections lie within tens of milliarcseconds of their VLA position some sources exhibit larger separations. For example, ONC105 (see Section 4 for source nomenclature) was detected at a signal-to-noise ratio (S/N) of 11 at a separation of 673.0 ± 0.5 mas, corresponding to approximately 260 AU at the distance of the ONC. These are plausibly associated with components of multiple systems and motivate the decision to not impose an angular separation cutoff during imaging.

[1]The website (http://astrogeo.org/) provides a catalogue of accurate positions for over 21 000 extragalactic sources with compact radio emission. The positions are updated four times a year, and the current catalogue, rfc_2026b, released on 2026 June 7, lists the position as
RA = $05^{h}41^{m}38.^{s}083373 \pm 0.^{s}000006$, Decl. = $-05^{\circ}41'49.''42861 \pm 0.''00018$.
[2]https://obs.vlba.nrao.edu/cst/

Downloaded from academic.oup.com/mnras/article/552/4/stag1806/8834038 by guest on 23 October 2026

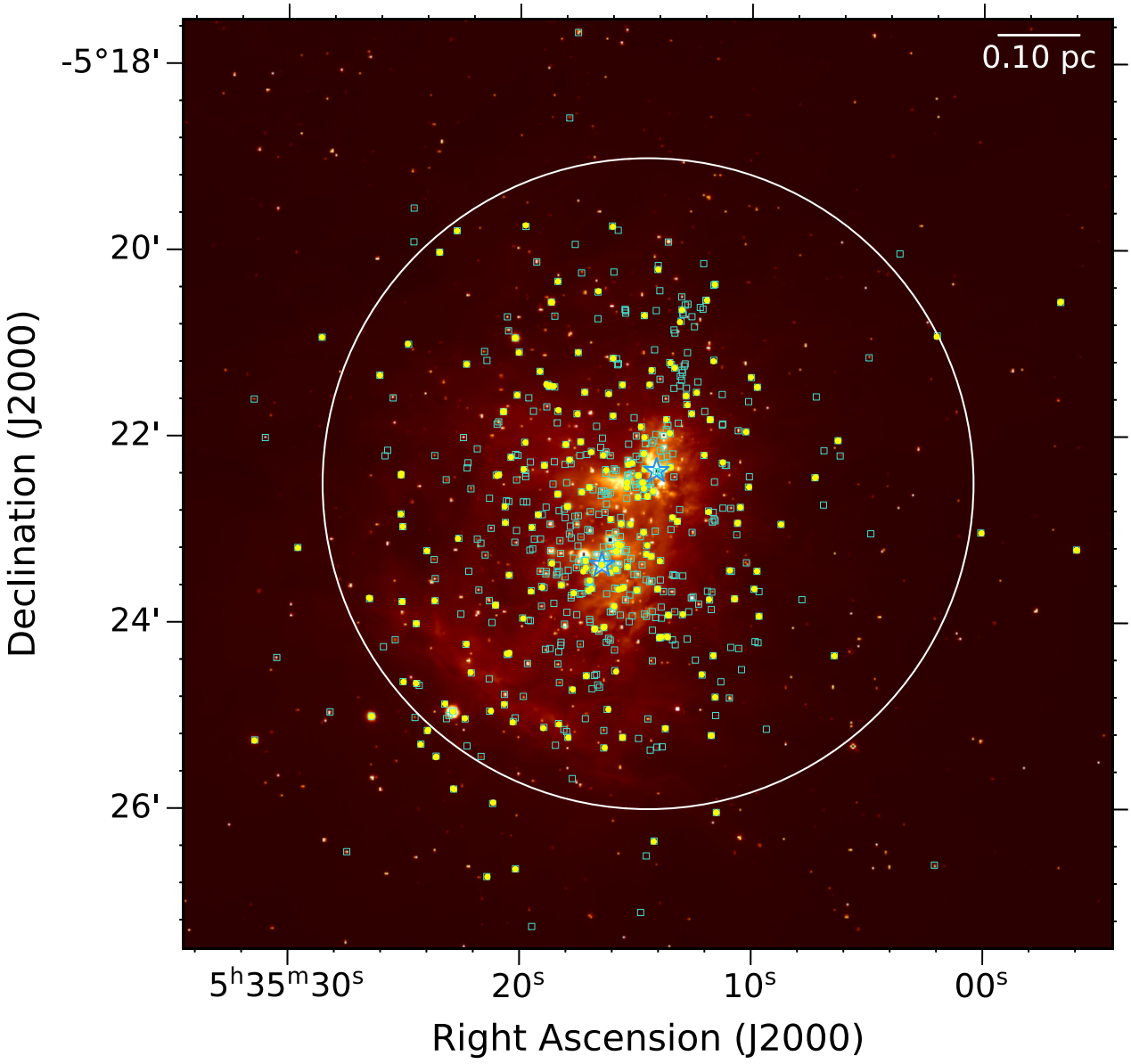


Figure 1. VISION 2.1 μm image of the ONC (S. Meingast et al. 2016). The phase centres are marked by the cyan squares, the VLBA source detections by yellow circles and the white circle is the FWHM size of the primary beam (∼7 arcmin). The cyan squares are 4 × 4 arcsec which corresponds to the larger (8192×8192) image size. The blue stars mark θ^1 Ori C (south) and the Becklin–Neugebauer Object (north).

The effective field-of-view in VLBI observations is limited by time and frequency smearing and therefore should be considered in the imaging strategy (J. M. Wrobel 1995). Frequency smearing arises because the visibilities measured over a finite bandwidth are gridded as if they were monochromatic, resulting in radial smearing of sources away from the phase centre and a decline in the peak response to a point source. As a consequence both angular resolution and sensitivity degrade with increasing distance from the phase centre. Time smearing also introduces amplitude losses for sources located away from the phase centre. These losses arise from the apparent motion of a source through the coherence pattern due to the Earth's rotation, such that averaging samples in time result in a reduction of measured peak flux density (e.g. J. M. Wrobel 1995; A. H. Bridle & F. R. Schwab 1999; M. A. Garrett et al. 1999).

For the observational setup used here the effective field-of-view is limited to FWHM of ≈5 arcsec due to time and frequency smearing (J. M. Wrobel 1995). These approximate limits inform the imaging size for this work. The overall imaging methodology described by J. Forbrich et al. (2021) is adopted in this work. The smallest synthesized beam size across the data set is 1.1 × 2.7 mas that was sampled with at least two pixels per half-power beamwidth in each axis. At the distance of the ONC this angular resolution corresponds to ∼0.4 AU. The coronae of young stars are expected to have sizes of up to tens of solar radii where K. V. Getman, E. D. Feigelson & G. P. Garmire (2021) estimate coronal extents in the range 0.5-10 $R_\odot$ ($10R_\odot \approx 0.05$ AU). Therefore, at this resolution the emission is expected to be unresolved.

The choice of signal-to-noise detection threshold was informed by the analyses presented by E. Middelberg et al. (2013) and N. Herrera Ruiz et al. (2017). However, the larger images produced

Downloaded from academic.oup.com/mnras/article/552/4/stag1806/8834038 by guest on 23 October 2026

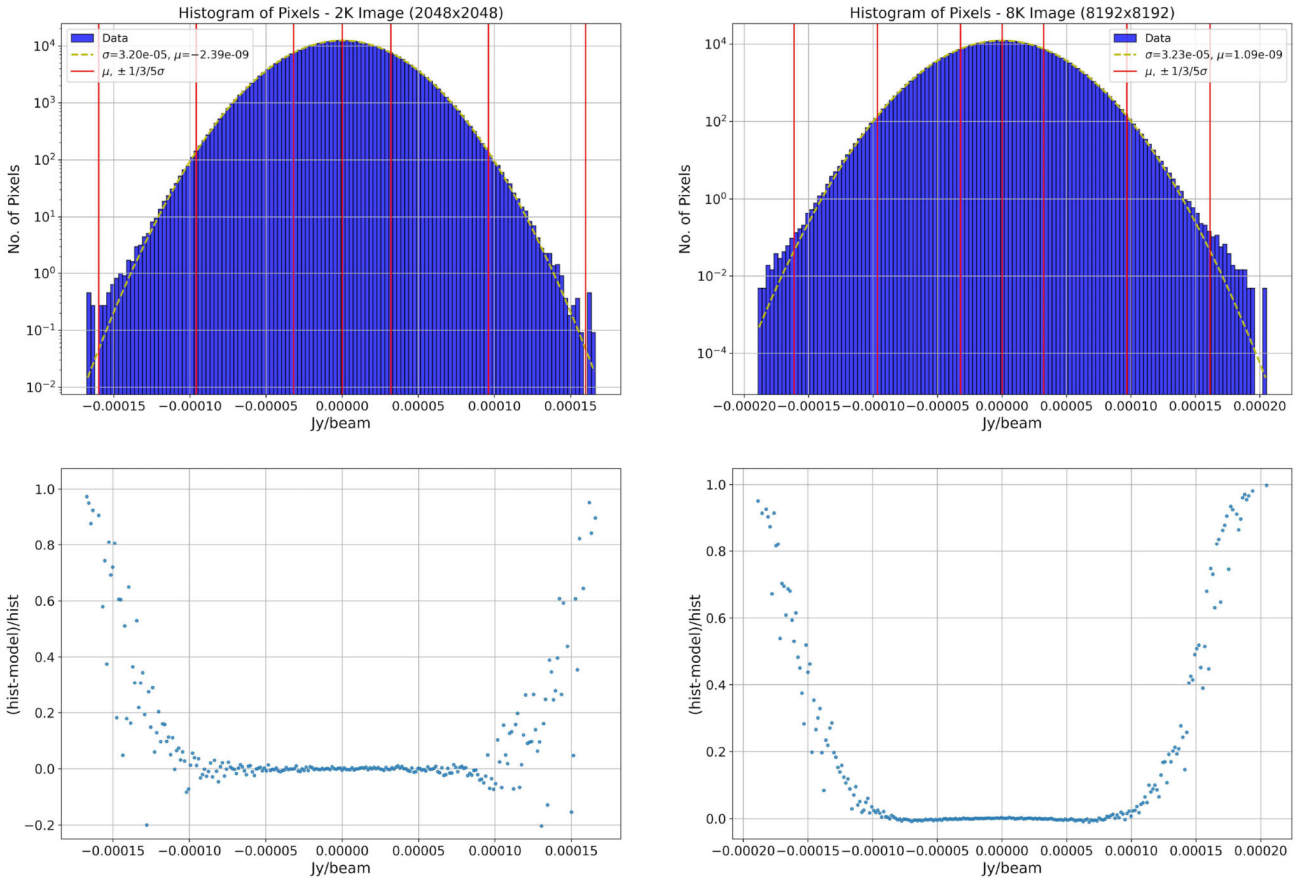


Figure 2. Histogram of the pixels for the 2K images (2048×2048) in left portion and the 8K images (8192×8192) in right portion. Upper panels show the histogram, a model distribution calculated from the pixel mean and standard deviation (yellow dashed line), and red vertical lines indicate the mean and $\pm1\sigma$, $\pm3\sigma$ and $\pm5\sigma$. The bottom panels show the residuals normalized to the histogram. The model shows that the high and low ends exhibit an excess of pixels. We quantify this as an excess kurtosis of 0.02 indicating the bulk is close to Gaussian and tail ratio at 5σ of ∼4.6 times more extreme pixels showing the significant deviations at the tails.

for this work have ∼67 million pixels which contain ∼4.9 million synthesized beam areas. This substantially larger search space increases the probability of false-positive detections and requires careful consideration of the detection threshold.

The expected number of false-positive detections per image was estimated using the number of independent synthesized beams and the Gaussian tail probability. A single image containing ∼4.9 million synthesized beam areas yields an expected number of false positives of ∼19 at 5σ, ∼0.003 at 6.5σ, and $\sim 8.6 \times 10^{-5}$ at 7σ. When scaled to all eight epochs yields an expected ∼0.3 false detections and a false positive rate of ∼0.4 sources at 7σ.

Fig. 2 presents a histogram of pixel values for both image sizes used in this work with a Gaussian model fitted using the measured pixel mean and standard deviation. The model assumes that the pixels approximately follow a Gaussian distribution. The red vertical lines indicate the mean and $\pm1\sigma$, $\pm3\sigma$, $\pm5\sigma$. The lower panel shows the residuals normalized to the histogram, revealing clear excesses at both low and high pixels values relative to a Gaussian distribution. The consistency between the two image sizes demonstrates that the observed non-Gaussian behaviour is present in the image pixel statistics and is not dependent on the adopted image size. To quantify the deviation we compute the excess kurtosis of 0.02 which indicates that the bulk distribution remains close to Gaussian, although the extreme tails show significant deviations. At the 5σ level the tail ratio is ∼4.6 times more extreme pixels than expected for the nominal Gaussian expectation and at 7σ this is effectively 0. This non-Gaussian behaviour implies that detection thresholds of $< 5.5\sigma$ are insufficient to identify detections. Consequently, to ensure a negligible false-positive rate in the presence of non-Gaussian noise we adopt a conservative threshold of 7σ.

E. Middelberg et al. (2013) also reported a similar non-Gaussian distribution of image noise in their wide-field VLBA observations. They investigated several different possible causes including different visibility weighting schemes and image averaging which did not resolve the behaviour, and were unable to identify an origin. Their observations were conducted at 1.382 GHz and our observations at 7.196 GHz exhibited similar non-Gaussian behaviour, indicating this could be occurring across different observing frequencies. However, we cannot establish whether the effects have the same underlying origin.

Peak candidates were initially identified using the peak pixel value and pixel rms measured with the AIPS task `imstat` (E. W. Greisen 2003). To further motivate the adoption of a high detection threshold we examined the distribution of peak

Downloaded from academic.oup.com/mnras/article/552/4/stag1806/8834038 by guest on 23 October 2026

signal-to-noise ratios in the images across the four new epochs. Every image in the fifth epoch contains at least one peak with S/N $\geq$ 5 and at S/N $\geq$ 5.5 a total of 238 peaks were found. The fifth epoch has 28 sources that are real detections (see below for further discussion) meaning that 210 of these are spurious, demonstrating that larger images introduce a substantial number of false-positives.

To ensure real sources were not missed due to elevated noise we also repeated the imaging strategy of J. Forbrich et al. (2021). This involved creating smaller undersampled images of 2048^2 pixels (approximately four million pixels total) which corresponds to between 120 000 and 270 000 synthesized beam areas. Candidate peaks in these images were again identified using `imstat` adopting a lower threshold of S/N $\geq$ 5.5. These smaller images significantly reduce statistical noise peaks but only allow imaging of a much smaller area of about one square arcsec. This dual search strategy ensures sensitivity to real sources while maintaining a low false-positive rate.

To summarize the source candidate search strategy two complementary imaging approaches were adopted. First, large undersampled images of 8192^2 pixels were searched using a conservative threshold of S/N $\geq$ 7. This yielded 189 peak candidates across the four new epochs. Second, to ensure that real detections were not missed due to elevated noise in the larger images, smaller undersampled images of 2048^2 pixels were also created and searched using a threshold of S/N $\geq$ 5.5 which yielded 122 peak candidates. This follows the methodology of J. Forbrich et al. (2021).

Once candidate peaks were identified oversampled images were created for each source candidate in Stokes *I*. These images were 2048^2 pixels with a pixel size of 0.05 mas, corresponding to an area of 0.1 $\times$ 0.1 arcsec or $\sim$1680 square AU at the distance of the ONC. This image size ensures that each source is fully contained within the imaged area accounting for positional uncertainties in the undersampled images. The pixel scale oversamples the smallest synthesized beam by a factor of 11 ensuring imaging aliasing is negligible. Source positions and flux densities were measured using the CASA task `imfit` which fits a two-dimensional Gaussian (CASA Team 2022). This task also provides other image statistics such as rms. The data has an average rms sensitivity of 35 μJy beam^{-1} and lowest rms of 21 μJy beam^{-1} across the four new epochs.

The final detection criteria were defined with the methodology from J. Forbrich et al. (2021) in mind, where they estimate for the oversampled images which are 2048^2 pixels in size that the expected number of false-positive detections is $\sim$0.1 sources across four epochs and the nominal Gaussian expectation is $\sim$0.02. To also maintain consistency with previous work and considering these noise characteristics for these smaller images we also adopt a threshold of S/N $\geq$ 6.5 in the measurements from `imfit` as our final detection threshold.

Source detection across multiple epochs is also complicated by variability and significant source proper motion. Non-thermal radio emission from YSOs is known to be highly variable (e.g. M. Güdel 2002; A. T. Deller, J. Forbrich & L. Loinard 2013; J. Forbrich et al. 2017, 2021) and the larger images used in this work introduce larger probabilities of statistical noise peaks. In addition, substantial proper motions are present in the ONC.

S. A. Dzib et al. (2021) report proper motions of YSOs within the ONC using the first four epochs of the data used in this work. They report proper motions of up to several milliarcsecond per year meaning sources can shift their position significantly and therefore coincident detections are not possible. As a result, detections are assessed on an epoch-by-epoch basis and associations between epochs are made using source identification from previous VLBA and VLA studies rather than positional coincidence alone.

If epochs are closely separated by at most several days then source proper motions are negligible and it is assumed that the source is effectively in the same position. This allows epochs that are closely spaced to be concatenated to improve sensitivity. This methodology was adopted by J. Forbrich et al. (2021) for the second and third epochs which are separated by 1 d. We extend this strategy by concatenating the fifth and sixth epochs that are separated by 4 d, and the seventh and eighth epochs separated by 1 d. In all other respects the imaging strategy for the concatenated data follows that described above.

Once a complete detection list was obtained for all epochs the measured peak flux densities were corrected for primary beam attenuation following R. P. Deane et al. (2024). The VLBA primary beam is well approximated by an Airy disc with an effective diameter of $D = 25.47$ m (E. Middelberg et al. 2013), assumed to be radially symmetric and normalized to unity at the pointing centre. For each source the attenuation factor was calculated from the angular offset at a central frequency of 7.196 GHz and the corresponding correction applied to all flux densities. As discussed by R. P. Deane et al. (2024) uncertainties become increasingly underestimated beyond the $\sim$ 80 per cent power point ($\sim$2.8 arcmin), where correction factors grow rapidly; these sources are flagged where appropriate but retained as detections considering their S/N $\geq$ 6.5.

This correction was not applied in the earlier papers in this series of S. A. Dzib et al. (2021) and J. Forbrich et al. (2021), whose analyses focused on detection statistics and astrometry. In contrast, our study requires corrected flux densities to derive radio luminosities for the Güdel–Benz investigation (see Section 4.6) and for a per-epoch variability analysis, motivating the application of a primary beam correction.

Finally, all confirmed source detections were also imaged in Stokes *V* to investigate circular polarization. These images were produced using the same oversampled imaging strategy described above.

3.1 Variability factor

The peak flux densities from `imfit` across multiple epochs allow an analysis of radio variability on the time-scales of the epoch spacing (see Table 1 for epoch dates). We use the variability factor (VF) to quantify source variability, which is defined as the ratio of the maximum to minimum *per-epoch* peak flux densities for a source. Larger values of VF indicate higher levels of variability (e.g. J. Vargas-González et al. 2023; J. Vargas-González 2024).

For sources detected in multiple epochs their VFs were calculated directly from the epoch-averaged peak flux density and uncertainties from standard error propagation of the individual flux density measurements. All the variability measurements in this work are significant with an S/N $\geq$ 3. This ensures that measured variability reflects intrinsic source behaviour rather than fluctuations within the uncertainty from image noise. For sources detected in only a single epoch lower limits of the VF were estimated by adopting 5.5σ of the lowest rms as an upper limit. This threshold was motivated by peaks of $\leq 5\sigma$ that are unreliable due to non-Gaussian noise properties as discussed in Section 3. Therefore, a more conservative threshold of 5.5σ is adopted for upper limit estimates.

Downloaded from academic.oup.com/mnras/article/552/4/stag1806/8834038 by guest on 23 October 2026

In this work we define higher variable sources as those exhibiting changes in their flux density by a factor of ≥ 5. This threshold was chosen empirically based on the distribution of inter-epoch VFs observed within the data set and lies well beyond statistical and calibration uncertainties; this also isolates distinct higher variability observed within the VF distribution.

4 RESULTS AND DISCUSSION

Throughout this section we use the term *source* to refer to a unique object and *detection* to denote an individual epoch in which a source is detected; this distinction avoids confusion for sources detected in multiple epochs. From a total of 575 targets we report 226 sources corresponding to 335 detections and an overall detection fraction of 39 per cent. As noted in Section 1 it is not expected that all VLA-detected sources could be detected by VLBA observations as some are known to be non-stellar in origin (e.g. J. Forbrich et al. 2016; J. Vargas-González et al. 2021). Most detected sources (188 sources, ∼83 per cent of unique sources) are detected in only a single epoch, while 35 sources (∼16 per cent) are detected in multiple epochs and of those 9 sources (∼4 per cent) are detected in all epochs. There are also 19 sources detected in subsequent closely spaced epochs. In addition to the 123 sources reported by J. Forbrich et al. (2021) we identify 59 sources from the four newly observed epochs and a further 34 sources detected only in the concatenated data, yielding a total of 93 sources. Among the detected sources 177 have S/N $\geq$ 10 and of these there are 46 sources that have S/N $\geq$ 20 and 10 sources that have S/N $\geq$ 50.

It should be highlighted that a significant number of VLA-detected sources remain undetected in the VLBA epochs. There are 349 sources (∼61 per cent) detected in the VLA data that are not detected in the VLBA epochs. The average rms sensitivity of the VLBA observations (∼35 μJy beam^{-1}) is roughly an order of magnitude higher than for the VLA data (∼3 μJy beam^{-1}) reported by J. Forbrich et al. (2016). If we assume the flux densities in the VLA data do not change there are 217 sources that are above the VLBA detection threshold of $S \geq 0.2$ mJy beam^{-1} (6.5σ of the average rms of the data) and of these there are 134 sources not detected in our VLBA data. However, this difference in source detection cannot solely be explained by this difference in sensitivity. Instead, this could represent a subset of VLA-detected sources lacking a compact non-thermal component, variability, the difference in sensitivity discussed above or a combination thereof. It should be highlighted that VLBA non-detections cannot be assumed to be thermal sources, as strong variability within the VLBA population means that some non-thermal sources may lie below the VLBA detection threshold during the epochs of our data. The source populations are also discussed by J. Forbrich et al. (2016) from their VLA observations.

The source identifiers are from the [FRM2016] catalogue presented by J. Forbrich et al. (2016) of 556 sources and are labelled as 'ONC' followed by their catalogue number. The 19 additional sources reported by J. Vargas-González et al. (2021) are appended sequentially to this catalogue; for example the first additional source is designated as 'ONC557'. We consider a source associated with the nominal VLA position when the angular separation is $\leq$ 800 mas. This threshold is motivated by the range of separations observed in our sample. For example, ONC105 is detected at S/N = 10.9 at a separation of 673.0 ± 0.5 mas (corresponding to ∼261 AU at the distance of the ONC).

There are detection candidates that are at larger separations of >800 mas, for example, there is a candidate for ONC229 within the sixth epoch at S/N = 19.5 at a separation of 1025.7 ± 0.1 mas (∼398 AU). This candidate has the highest signal-to-noise of these potential candidates. Sources at such large separations from their respective phase centre could indicate a binary nature to these systems or coincident alignments of unrelated sources. These detection candidates found at larger separations are discussed in Appendix A.

We also identify cases where multiple VLBA sources associated with the same phase centre are detected. In total 26 such sources are identified and listed in Tables 2 and 3. Sources are classified as separate when their angular separations are too large to be explained by plausible proper motions or when multiple components are detected simultaneously within the same image. In these cases they are numbered sequentially based on the order they are detected (e.g. ONC002.1 is detected first within the third epoch and ONC002.2 is detected second within the fourth epoch). Where sources are detected simultaneously that have not been detected previously the brightest source (i.e. the highest peak flux density) is designated as the 'first' source. For example, ONC427 is detected simultaneously as two separate sources and neither have previously been detected; therefore the source with the higher flux density is designated as ONC427.1 and the other source as ONC427.2.

Four source pairs are detected within the same image: ONC177 in epoch 4 at a separation of 22.9 ± 0.3 mas (∼9 AU), ONC413 in the concatenated epoch of BF131AB at a separation of 16.6 ± 0.4 mas (∼6 AU), ONC414 in epoch 4 at a separation of 168.2 ± 0.3 mas (∼ 65 AU) and ONC427 in epoch 7 at a separation of 16.6 ± 0.4 mas (∼6 AU). We note it is currently unknown whether these sources are gravitationally bound. These sources will be discussed in more detail in a future astrometry paper.

4.1 Circular polarization

Stokes V images were created for all detections in each epoch to search for circular polarization. Previous work has only occasionally detected circular polarization; for example L. A. Zapata et al. (2004a) detect varying circular polarization from 4 to 10 per cent associated with one of the 77 sources (associated with ONC066 or GMR A) detected across their four VLA observing epochs at 3.6 cm. L. A. Zapata et al. (2004b) also detected approximately 20 per cent circular polarization from one of the 11 sources (associated with ONC154 or their source 140-410) in their VLA observations at 1.3 cm wavelength. These measurements provide useful comparisons, although the VLA and VLBA have different spatial sensitivities and probe different angular scales, in addition to differences in observing frequency and sensitivity.

No significant Stokes V detections were identified within our VLBA sample. Therefore, upper limits on the fractional circular polarization were estimated using the rms of the Stokes V images, following n $\sigma_V / I_{\rm peak}$, where $n = 5.5$, σ_V is the Stokes V rms and $I_{\rm peak}$ is the Stokes I peak flux density. The resulting upper limits span a wide range from 1 up to 100 per cent with a median upper limit of ∼13 per cent. Upper limits approaching 100 per cent do not imply highly circular polarized emission, rather they indicate the source is too faint relative to the Stokes V noise for a meaningful constraint. The best constrained upper limit is associated with the brightest detection in our data of ONC254 in the first epoch with an upper limit of ∼1 per cent. For ONC066 our 5.5σ upper limits on the fractional circular polarization range

Downloaded from academic.oup.com/mnras/article/552/4/stag1806/8834038 by guest on 23 October 2026

Table 2. Table of primary beam-corrected flux density measurements in mJy beam^{-1} from the resulting `imfit` (CASA Team 2022) and the inter-epoch variability factors for each VLBA epoch.

[FRM2016]	COUP	BF117 [2015-10-26]	BF123A [2017-10-26]	BF123B [2017-10-27]	BF123C [2018-10-26]	BF131A [2020-10-25]	BF131B [2020-10-29]	BF131C [2021-10-30]	BF131D [2021-10-31]	Variability factor
002.1[a]	107	-	-	0.29 ± 0.02	-	-	-	-	-	>1.2
002.2[a]	107	-	-	-	2.80 ± 0.07	2.01 ± 0.07	1.38 ± 0.04	-	-	2.0 ± 0.1
003.1[a]	-	-	-	-	-	-	-	0.75 ± 0.08	-	>6.1
003.2[a]	-	-	-	-	-	-	-	-	0.45 ± 0.06	>3.7
004	141	-	-	-	-	-	-	-	0.37 ± 0.03	>2.1
005	172	-	-	-	-	-	-	0.41 ± 0.04	-	>2.2
010.1	262	-	-	-	0.29 ± 0.01	-	0.25 ± 0.02	-	-	1.2 ± 0.1
010.2	262	-	-	-	-	0.24 ± 0.02	-	-	-	>2.0
011	-	-	-	0.26 ± 0.01	-	-	-	-	-	>1.5
014.1	283	-	0.17 ± 0.02	-	-	-	-	-	-	>1.4
014.2	283	-	-	-	-	-	-	-	0.17 ± 0.01	>1.4
016	322	-	-	-	-	1.56 ± 0.03	-	-	-	>12.5
018	338	0.62 ± 0.03	0.15 ± 0.03	-	-	-	-	-	-	3.9 ± 0.6
022	342	0.23 ± 0.02	-	0.40 ± 0.03	-	0.21 ± 0.01	-	-	-	1.9 ± 0.2
024	350	0.19 ± 0.01	-	-	-	-	-	-	-	>1.4
030	363	-	0.16 ± 0.02	-	-	-	-	-	-	>1.3
035	390	-	-	-	-	0.28 ± 0.02	-	-	-	>2.3
037	394	-	-	0.19 ± 0.01	-	-	-	0.38 ± 0.02	0.30 ± 0.01	1.9 ± 0.2
042	-	-	-	-	0.17 ± 0.01	-	-	-	-	>1.2
051[a]	430	-	-	-	-	1.06 ± 0.05	0.53 ± 0.05	-	-	1.9 ± 0.2
053	427	-	-	-	0.37 ± 0.02	-	-	-	-	>1.8
055	-	-	-	0.24 ± 0.02	-	-	-	-	-	>1.4
059	434	-	-	-	-	-	-	-	0.16 ± 0.01	>1.1
064	444	0.48 ± 0.03	-	0.27 ± 0.03	-	-	0.68 ± 0.04	-	-	2.5 ± 0.2
066	450	1.33 ± 0.05	1.99 ± 0.03	1.16 ± 0.02	1.39 ± 0.02	5.55 ± 0.11	2.05 ± 0.06	10.29 ± 0.18	3.34 ± 0.12	8.8 ± 0.2
068	-	-	-	-	-	-	-	0.18 ± 0.02	-	>1.5
070	454	-	-	0.25 ± 0.02	-	-	-	-	-	>1.6
072	-	-	-	0.15 ± 0.01	-	-	-	-	-	>1.3
075.1	465	-	-	-	0.18 ± 0.01	-	-	-	-	>1.5
075.2	465	-	-	-	-	-	-	-	0.20 ± 0.02	>1.7
079	476	-	-	-	-	-	-	-	0.13 ± 0.01	>1.1
091	-	-	-	-	-	-	-	-	0.16 ± 0.02	>1.3
093	504	1.17 ± 0.11	-	-	-	-	-	0.32 ± 0.02	-	3.6 ± 0.4
098	510	0.24 ± 0.02	-	-	-	-	-	-	-	>1.7
102	-	-	-	-	-	-	-	0.29 ± 0.03	-	>1.9
105	-	-	-	-	-	-	0.22 ± 0.02	-	-	>1.5
110	530	-	-	-	-	0.52 ± 0.02	-	0.38 ± 0.02	0.14 ± 0.02	3.6 ± 0.5
122	-	-	-	0.13 ± 0.02	-	-	-	-	-	>1.1
127.1	551	-	-	0.14 ± 0.01	-	-	-	-	-	>1.2
127.2	551	-	-	-	-	-	-	0.16 ± 0.02	-	>1.4
129	-	-	-	0.18 ± 0.01	-	-	-	-	-	>1.3

Downloaded from academic.oup.com/mnras/article/552/4/stag1806/8834038 by guest on 23 October 2026

Table 2 – *continued*

[FRM2016]	COUP	BF117 [2015-10-26]	BF123A [2017-10-26]	BF123B [2017-10-27]	BF123C [2018-10-26]	BF131A [2020-10-25]	BF131B [2020-10-29]	BF131C [2021-10-30]	BF131D [2021-10-31]	Variability factor
130	554	0.26 ± 0.03	0.88 ± 0.02	2.95 ± 0.05	8.27 ± 0.22	0.18 ± 0.02	-	-	-	47.1 ± 6.4
133.1	-	-	-	0.17 ± 0.02	-	-	-	-	-	>1.5
133.2	-	-	-	-	-	-	-	0.31 ± 0.02	-	>2.7
135	571	-	0.16 ± 0.01	-	-	-	-	-	-	>1.3
137	-	-	-	0.23 ± 0.02	0.19 ± 0.02	-	-	-	-	1.2 ± 0.1
148	593	-	0.17 ± 0.01	-	-	-	-	-	-	>1.4
154	594	0.65 ± 0.02	-	0.24 ± 0.01	1.94 ± 0.04	0.20 ± 0.02	-	-	0.16 ± 0.02	12.0 ± 1.9
158	602	-	0.18 ± 0.01	-	0.15 ± 0.01	-	-	-	-	1.1 ± 0.1
161	598	0.26 ± 0.03	-	-	-	-	-	-	-	>1.5
167[a]	608	-	-	-	0.46 ± 0.03	-	-	-	-	>1.0
170	622	-	-	-	0.13 ± 0.01	-	-	-	-	>1.0
176	-	-	-	-	0.14 ± 0.01	-	-	-	-	>1.0
177.1	625	0.22 ± 0.02	-	-	0.15 ± 0.01	-	-	-	-	1.5 ± 0.2
177.2	625	-	-	-	0.53 ± 0.01	-	-	-	0.22 ± 0.01	2.4 ± 0.2
182	-	-	-	0.19 ± 0.01	-	-	-	-	-	>1.5
184	639	0.19 ± 0.02	0.41 ± 0.02	0.24 ± 0.01	0.93 ± 0.02	5.19 ± 0.08	1.53 ± 0.04	1.21 ± 0.02	0.60 ± 0.03	27.3 ± 2.9
188	-	-	0.17 ± 0.01	-	-	-	-	-	-	>1.4
189	640	0.20 ± 0.02	-	-	-	-	-	-	-	>1.7
193	-	-	-	-	-	-	-	0.18 ± 0.02	-	>1.6
194	-	-	-	-	-	-	-	-	0.14 ± 0.01	>1.2
196	648	0.69 ± 0.03	-	-	-	-	-	-	-	>6.0
197	645	-	0.19 ± 0.01	-	-	-	-	-	-	>1.3
198	647	-	-	0.17 ± 0.02	0.17 ± 0.01	-	-	-	-	1.0 ± 0.1
199	649	-	-	-	-	0.34 ± 0.02	-	-	0.11 ± 0.01	3.0 ± 0.3
203	655	-	-	-	-	-	0.19 ± 0.01	-	-	>1.6
205	-	0.17 ± 0.02	-	-	-	-	-	-	-	>1.5
211	662	0.19 ± 0.02	0.56 ± 0.01	0.56 ± 0.02	0.14 ± 0.01	-	-	-	-	4.0 ± 0.3
212	670	1.06 ± 0.02	-	-	-	-	-	-	-	>9.2
219	680	-	-	-	-	-	-	-	-	-
222	689	-	-	0.17 ± 0.01	-	-	-	-	0.62 ± 0.03	>5.3
227	-	-	-	0.13 ± 0.01	-	-	-	-	-	>1.4
229	-	0.21 ± 0.02	-	-	-	-	-	-	-	>1.0
230	-	-	-	-	0.12 ± 0.01	-	-	-	-	>1.7
232	-	-	-	-	0.13 ± 0.01	-	-	-	-	>1.0
240	717	0.23 ± 0.01	-	-	-	-	-	-	-	>1.0
241	718	1.57 ± 0.07	1.18 ± 0.02	0.22 ± 0.02	2.12 ± 0.03	2.99 ± 0.07	0.83 ± 0.05	1.86 ± 0.05	1.08 ± 0.04	>1.9
243	-	-	-	-	-	-	-	-	0.12 ± 0.01	13.5 ± 1.2
244.1	724	-	-	-	-	-	0.33 ± 0.02	-	-	>1.0
244.2	724	-	-	-	-	-	-	0.19 ± 0.01	-	>2.8
										>1.6

Downloaded from academic.oup.com/mnras/article/552/4/stag1806/8834038 by guest on 23 October 2026

Table 2 – *continued*

[FRM2016]	COUP	BF117 [2015-10-26]	BF123A [2017-10-26]	BF123B [2017-10-27]	BF123C [2018-10-26]	BF131A [2020-10-25]	BF131B [2020-10-29]	BF131C [2021-10-30]	BF131D [2021-10-31]	Variability factor
249	734	-	-	-	0.13 ± 0.01	-	-	-	-	>1.0
250	732	1.99 ± 0.02	1.39 ± 0.02	2.58 ± 0.04	2.52 ± 0.05	4.40 ± 0.10	2.05 ± 0.07	4.62 ± 0.07	2.74 ± 0.09	3.3 ± 0.1
254	745	42.72 ± 0.87	9.14 ± 0.08	1.77 ± 0.04	32.23 ± 0.32	13.42 ± 0.26	18.03 ± 0.32	6.37 ± 0.09	7.23 ± 0.25	24.0 ± 0.6
260	-	-	-	-	-	-	0.17 ± 0.02	-	-	>1.1
267	763	0.20 ± 0.02	-	-	-	-	-	-	-	>1.6
268	762	-	-	-	-	-	-	-	0.16 ± 0.02	>1.2
270	760	-	-		-	0.28 ± 0.02	-	-	-	>1.3
273	-	-	-	-	0.15 ± 0.01	-	-	-	-	>1.0
274	765	-	-	-	-	-	-	-	0.14 ± 0.01	>1.2
300.1	801	0.20 ± 0.02	-	-	-	-	-	-	-	>1.7
300.2	801	-	-	-	-	-	0.97 ± 0.04	-	-	>8.2
303	806	-	-	0.15 ± 0.01	-	-	-	-	-	>1.2
305	809	-	-	-	-	-	-	-	0.24 ± 0.02	>2.0
314	-	0.30 ± 0.03	-	-	-	-	-	-	-	>1.9
319	828	0.54 ± 0.04	0.33 ± 0.02	0.17 ± 0.01	0.16 ± 0.01	0.41 ± 0.01	0.26 ± 0.02	0.53 ± 0.02	0.36 ± 0.02	3.4 ± 0.3
321	827	-	0.21 ± 0.01	-	-	-	-	-	-	>1.7
325	847	-	-	-	-	-	-	0.22 ± 0.01	-	>1.7
326	841	-	-	0.21 ± 0.01	-	-	-	-	-	>1.8
327	855	0.21 ± 0.02	-	-	-	-	-	-	-	>1.6
334	854	-	-	-	-	1.20 ± 0.02	0.38 ± 0.02	-	-	3.1 ± 0.2
335	856	-	0.16 ± 0.01	-	-	-	-	-	-	>1.3
339.1	-	-	-	-	0.17 ± 0.01	-	-	-	-	>1.4
339.2	-	-	-	-	-	-	-	0.31 ± 0.03	-	>2.7
340	-	-	-	-	-	-	0.16 ± 0.02	-	-	>1.3
343	867	0.22 ± 0.02	-	-	-	-	-	-	-	>1.7
344	-	-	-	-	-	-	0.19 ± 0.02	-	-	>1.5
347	876	-	-	-	0.13 ± 0.01	-	-	-	-	>1.0
350	874	0.20 ± 0.01	0.14 ± 0.01	-	0.28 ± 0.01	-	0.17 ± 0.02	-	-	1.6 ± 0.2
360	897	-	-	0.14 ± 0.01	-	-	-	-	-	>1.2
364	912	-	-	0.20 ± 0.01	-	-	-	-	-	>1.5
367	-	-	0.23 ± 0.01	-	-	-	-	-	-	>1.3
377[a]	-	-	-	-	-	-	-	-	0.28 ± 0.03	>1.3
378	932	6.77 ± 0.15	3.30 ± 0.06	2.06 ± 0.03	4.48 ± 0.09	0.31 ± 0.02	4.76 ± 0.15	0.55 ± 0.03	0.44 ± 0.02	22.0 ± 1.5
382	942	0.15 ± 0.02	-	-	0.29 ± 0.02	-	-	-	-	2.0 ± 0.3
389	956	0.18 ± 0.02	-	-	-	-	-	-	-	>1.4
398	-	-	-	-	0.23 ± 0.02	-	-	-	-	>1.0
400	965	5.86 ± 0.14	2.11 ± 0.06	3.08 ± 0.06	14.40 ± 0.32	4.09 ± 0.08	12.53 ± 0.37	7.13 ± 0.12	8.83 ± 0.30	6.8 ± 0.3
402	963	-	-	-	0.18 ± 0.02	-	-	-	-	>1.0
408	-	-	-	0.16 ± 0.02	-	-	-	-	-	>1.2
414.1	985	0.70 ± 0.07	0.19 ± 0.03	-	0.15 ± 0.01	-	-	-	-	4.5 ± 0.6
414.2	985	-	-	0.41 ± 0.02	0.54 ± 0.02	-	-	-	-	1.3 ± 0.1

Downloaded from academic.oup.com/mnras/article/552/4/stag1806/8834038 by guest on 23 October 2026

Table 2 – *continued*

[FRM2016]	COUP	BF117 [2015-10-26]	BF123A [2017-10-26]	BF123B [2017-10-27]	BF123C [2018-10-26]	BF131A [2020-10-25]	BF131B [2020-10-29]	BF131C [2021-10-30]	BF131D [2021-10-31]	Variability factor
418	-	-	-	-	-	-	-	-	0.16 ± 0.01	>1.2
419	-	-	-	-	-	-	-	0.28 ± 0.02	-	>2.1
426[a]	-	-	-	0.25 ± 0.03	-	-	-	-	-	>1.2
427.1	1008	-	-	-	-	-	-	0.18 ± 0.02	-	>1.5
427.2	1008	-	-	-	-	-	-	0.16 ± 0.01	-	>1.3
430	-	-	-	-	-	-	-	0.26 ± 0.03	-	>1.9
434	1016	-	-	-	-	-	-	0.28 ± 0.02	-	>2.1
435	1023	-	-	0.29 ± 0.02	-	0.13 ± 0.01	-	-	-	2.1 ± 0.2
440	-	-	-	-	0.14 ± 0.01	-	-	-	-	>1.0
441	-	-	-	-	-	-	-	0.29 ± 0.02	-	>2.2
444.1[a]	1035	-	-	-	-	-	4.82 ± 0.55	-	-	>32.4
444.2[a]	1035	-	-	-	-	-	-	-	4.58 ± 0.32	>30.8
452	-	-	-	-	-	-	-	0.26 ± 0.02	-	>2.1
453	1056	-	-	-	-	-	-	0.22 ± 0.02	-	>1.8
456	-	-	-	0.18 ± 0.01	-	-	-	-	-	>1.3
457	1071	-	0.17 ± 0.01	-	-	-	-	-	-	>1.2
459	1083	0.65 ± 0.02	-	-	-	-	-	-	-	>4.9
462[a]	1087	-	-	-	0.32 ± 0.01	-	-	-	-	>2.5
466	1090	-	0.31 ± 0.01	1.14 ± 0.03	-	-	-	-	-	3.7 ± 0.2
467[a]	1091	-	-	0.26 ± 0.01	-	-	-	-	-	>1.2
468	1100	-	-	-	0.22 ± 0.01	-	-	-	-	>1.6
469	1101	-	-	-	-	-	-	-	0.19 ± 0.01	>1.4
470	-	-	-	-	0.17 ± 0.01	-	-	-	-	>1.0
476	-	-	-	-	-	0.21 ± 0.02	-	-	-	>1.6
477	1110	-	-	-	0.13 ± 0.01	-	-	-	-	>1.0
478[a]	-	-	-	-	-	-	-	0.34 ± 0.03	-	>1.7
480	1116	0.22 ± 0.01	-	-	0.47 ± 0.02	0.19 ± 0.02	-	1.24 ± 0.04	1.19 ± 0.04	6.5 ± 0.4
485	1130	1.15 ± 0.05	0.35 ± 0.01	0.87 ± 0.02	0.61 ± 0.01	1.50 ± 0.03	1.20 ± 0.05	0.57 ± 0.05	0.28 ± 0.02	5.5 ± 0.5
486[a]	1139	-	-	-	-	-	-	-	0.52 ± 0.05	>1.5
493[a]	1151	-	-	-	-	-	-	0.21 ± 0.02	-	>1.8
501	1184	-	0.23 ± 0.01	-	-	-	-	-	-	>1.3
507	-	-	-	-	-	-	-	0.25 ± 0.01	-	>1.7
508	1205	-	-	-	0.18 ± 0.01	-	-	-	-	>1.0
509[a]	-	-	-	-	0.25 ± 0.01	-	-	-	-	>1.0
512	-	-	-	0.17 ± 0.01	-	-	-	-	-	>1.3
513[a]	1224	-	-	-	-	0.61 ± 0.03	-	-	-	>2.6
514[a]	-	-	-	0.43 ± 0.02	-	-	-	-	-	>1.3
515[a]	1232	-	-	-	0.22 ± 0.02	-	-	-	-	>1.0
519[a]	-	-	-	-	-	-	-	0.41 ± 0.03	-	>1.9
520[a]	1249	-	-	-	0.32 ± 0.02	-	-	1.00 ± 0.06	0.33 ± 0.02	3.1 ± 0.3
521.1[a]	1262	0.45 ± 0.05	-	-	-	-	-	-	-	>3.7
521.2[a]	1262	-	-	-	-	-	0.64 ± 0.02	-	-	>5.2

Downloaded from academic.oup.com/mnras/article/552/4/stag1806/8834038 by guest on 23 October 2026

Table 2 – *continued*

[FRM2016]	COUP	BF117 [2015-10-26]	BF123A [2017-10-26]	BF123B [2017-10-27]	BF123C [2018-10-26]	BF131A [2020-10-25]	BF131B [2020-10-29]	BF131C [2021-10-30]	BF131D [2021-10-31]	Variability factor
522	1260	-	-	0.28 ± 0.02	-	-	-	-	-	>1.8
525.1[a]	1275	-	0.34 ± 0.04	-	-	-	-	-	-	>2.8
525.2[a]	1275	-	-	-	-	-	-	-	0.35 ± 0.02	>2.9
526	1276	0.23 ± 0.02	-	-	-	-	-	-	-	>1.6
527[a]	1281	-	-	0.40 ± 0.02	-	-	-	-	-	>1.4
529[a]	1290	-	-	-	-	0.27 ± 0.03	-	-	-	>1.3
530[a]	1289	-	-	-	0.18 ± 0.02	-	-	-	-	>1.0
534[a]	-	-	-	0.29 ± 0.02	-	-	-	-	-	>1.7
535[a]	1313	-	-	-	0.23 ± 0.02	-	-	-	-	>1.0
536	1309	-	-	-	-	-	-	-	0.17 ± 0.01	>1.2
537.1[a]	1311	-	0.38 ± 0.02	-	-	-	-	-	-	>3.2
537.2[a]	1311	-	-	-	-	-	-	0.37 ± 0.02	-	>3.2
538.1	1314	-	0.25 ± 0.02	-	-	-	-	-	-	>2.1
538.2	1314	-	-	-	-	0.19 ± 0.02	-	-	-	>1.6
539	-	-	-	-	-	-	-	0.33 ± 0.03	-	>2.3
545[a]	1341	-	-	-	-	-	-	0.30 ± 0.03	-	>1.9
546[a]	1350	-	-	-	-	-	-	-	0.22 ± 0.01	>1.9
547[a]	1360	-	-	0.36 ± 0.02	-	-	-	-	-	>3.1
548.1[a]	1359	0.34 ± 0.02	-	-	-	-	-	-	-	>2.9
548.2[a]	1359	-	-	-	-	0.34 ± 0.03	-	-	-	>2.9
551[a]	-	-	-	-	-	-	-	-	0.39 ± 0.03	>2.0
552.1[a]	1428	-	-	0.26 ± 0.02	-	-	-	-	-	>2.2
552.2[a]	1428	-	-	-	-	-	-	0.42 ± 0.03	-	>3.5
555[a]	1473	-	0.50 ± 0.08	-	-	-	-	-	-	>4.2
556[a]	1550	-	-	-	-	-	-	0.31 ± 0.03	-	>2.7
557	672	-	-	0.30 ± 0.02	0.12 ± 0.01	-	-	-	-	2.5 ± 0.3
574	-	-	-	-	-	-	-	0.21 ± 0.02	-	>1.6

Notes. Columns are left to right: FRM2016 source number, COUP number, epoch names and dates and the variability factor (where they are quoted as greater than represents a lower limit).
[a]Source is outside the $\sim$ 80 per cent power point of the FWHM and the uncertainties might be underestimated.

Downloaded from academic.oup.com/mnras/article/552/4/stag1806/8834038 by guest on 23 October 2026

Table 3. Table of source detections for all eight VLBA epochs.

[FRM2016]	Epoch	COUP	Flux density (mJy beam^{-1})	S/N	α_{J2000}	σ_α (mas)	δ_{J2000}	σ_δ (mas)	$\Delta\theta$ (mas)	YSO class	Spectral type
ONC002.1[a]	3	107	0.29 ± 0.02	12.3	05:34:55.975453	0.144	−05:23:13.02408	0.237	156.8 ± 0.4	III	K1-K4
ONC002.2[a]	4	107	2.80 ± 0.07	41.1	05:34:55.974463	0.110	−05:23:13.03819	0.120	173.0 ± 0.1	III	K1-K4
ONC002.2[a]	5	107	2.02 ± 0.07	27.9	05:34:55.974645	0.120	−05:23:13.03824	0.125	172.6 ± 0.1	III	K1-K4
ONC002.2[a]	6	107	1.38 ± 0.04	34.5	05:34:55.974669	0.117	−05:23:13.03836	0.125	172.6 ± 0.1	III	K1-K4
ONC003.1[a]	7	—	0.75 ± 0.08	8.9	05:34:56.702516	0.163	−05:20:33.40197	0.194	159.6 ± 0.6		
ONC003.2[a]	8	—	0.45 ± 0.06	7.4	05:34:56.687174	0.280	−05:20:32.92400	0.423	441.1 ± 6.8		
ONC004[a]	8	141	0.37 ± 0.04	10.5	05:35:00.087741	0.129	−05:23:02.12618	0.233	274.5 ± 0.4	II	
ONC005[a]	7	172	0.41 ± 0.04	10.2	05:35:02.033498	0.124	−05:20:55.59794	0.221	567.8 ± 0.5		
ONC010.1	4	262	0.29 ± 0.01	27.9	05:35:06.283553	0.111	−05:22:02.66559	0.129	23.3 ± 0.1	III	K5
ONC010.2	5	262	0.24 ± 0.02	9.6	05:35:06.280761	0.125	−05:22:02.73416	0.224	96.5 ± 0.1	III	K5
ONC010.1	6	262	0.25 ± 0.02	10.8	05:35:06.283604	0.116	−05:22:02.66651	0.187	24.1 ± 0.1	III	K5
ONC011	3	—	0.26 ± 0.01	22.7	05:35:06.416899	0.123	−05:24:21.34737	0.182	173.9 ± 0.2		
ONC014.1	2	283	0.17 ± 0.02	10.3	05:35:07.243905	0.154	−05:22:26.30108	0.358	378.2 ± 1.1		M4.5
ONC014.2	8	283	0.17 ± 0.01	15.1	05:35:07.274686	0.111	−05:22:26.67022	0.149	117.8 ± 0.1		M4.5
ONC016	5	322	1.56 ± 0.03	52.2	05:35:08.736869	0.110	−05:22:56.69107	0.114	19.8 ± 0.1		M1.5
ONC018	1	338	0.62 ± 0.03	20.7	05:35:09.675505	0.123	−05:23:55.91207	0.176	41.8 ± 0.1		
ONC018	2	338	0.15 ± 0.03	5.4	05:35:09.676613	0.203	−05:23:55.93909	0.448	67.7 ± 0.5		
ONC021	A	343	0.15 ± 0.01	13.2	05:35:09.769718	0.127	−05:23:26.88885	0.276	7.5 ± 0.1	III	K4-M0
ONC022	1	342	0.23 ± 0.02	10.4	05:35:09.770302	0.149	−05:21:28.34616	0.269	9.5 ± 0.1		M0, K5-K7
ONC022	3	342	0.40 ± 0.03	15.5	05:35:09.769963	0.121	−05:21:28.34776	0.170	11.5 ± 0.1		M0, K5-K7
ONC022	5	342	0.21 ± 0.01	14.1	05:35:09.769547	0.113	−05:21:28.35828	0.163	22.7 ± 0.1		M0, K5-K7
ONC024	1	350	0.18 ± 0.01	14.8	05:35:09.882650	0.128	−05:23:38.33139	0.225	215.0 ± 0.3		
ONC025	A	—	0.11 ± 0.01	11.7	05:35:10.043950	0.126	−05:21:21.93646	0.256	223.0 ± 0.3		
ONC028	C	358	0.13 ± 0.01	8.9	05:35:10.121295	0.114	−05:22:32.64849	0.191	243.7 ± 0.1		M2
ONC030	2	363	0.16 ± 0.02	9.5	05:35:10.252282	0.157	−05:21:57.11306	0.269	144.0 ± 0.5		M5.5
ONC032	A	378	0.11 ± 0.01	9.6	05:35:10.494702	0.140	−05:22:45.75138	0.238	15.9 ± 0.1		
ONC035.1	A	390	0.11 ± 0.01	14.8	05:35:10.597707	0.138	−05:22:55.66422	0.261	393.9 ± 0.7		
ONC035.2	5	390	0.28 ± 0.02	13.9	05:35:10.615765	0.113	−05:22:56.05438	0.160	32.5 ± 0.1		
ONC037	3	394	0.19 ± 0.01	26.1	05:35:10.736699	0.115	−05:23:44.72561	0.148	72.9 ± 0.1		K2-M0
ONC037	7	394	0.38 ± 0.02	16.4	05:35:10.731601	0.116	−05:23:44.66254	0.161	24.3 ± 0.1		K2-M0
ONC037	8	394	0.30 ± 0.01	20.5	05:35:10.731600	0.111	−05:23:44.66283	0.134	24.4 ± 0.1		K2-M0

Notes. This table is available online in its entirety for download. A portion is shown here.
Columns are (left to right): source number (from J. Forbrich et al. 2016), epoch number, COUP number (from K. V. Getman et al. 2005), flux density, J2000 right ascension and declination, both with uncertainties, total separation from the phase centre, YSO class (from L. Prisinzano et al. 2008), spectral type (from L. A. Hillenbrand, A. S. Hoffer & G. J. Herczeg 2013).
The separations are: $\Delta\alpha = (\alpha_{\rm VLBA} - \alpha_{\rm PC} \cdot \cos\delta)$, $\Delta\delta = (\delta_{\rm VLBA} - \delta_{\rm PC})$, and $\Delta\theta = \sqrt{\Delta\alpha^2 + \Delta\delta^2}$, where 'VLBA' is the detected source position and 'PC' is the respective phase centre.
Epoch numbers are: 1 = BF117, 2 = BF123A, 3 = BF123B, 4 = BF123C, 5 = BF131A, 6 = BF131B, 7 = BF131C, 8 = BF131D, A = BF123AB, B = BF131AB, C = BF131CD.
[a]Source is outside the ∼ 80 per cent power point of the FWHM and the uncertainties might be underestimated.

Downloaded from academic.oup.com/mnras/article/552/4/stag1806/8834038 by guest on 23 October 2026

from 2 to 12 per cent and therefore do not exclude the 4 to 10 per cent circular polarization previously detected by L. A. Zapata et al. (2004a). Similarly, our upper limits for ONC154 range from 7 to 73 per cent, compatible with the ∼ 20 per cent circular polarization reported by L. A. Zapata et al. (2004b).

Therefore, the absence of Stokes V detections does not rule out gyrosynchrotron emission or circular polarization and still provides a constraint on the degree of polarization for sources with better-constrained upper limits. It is also worth highlighting that circular polarization can be highly variable and would only represent a fractional percentage of the total intensity (e.g. G. A. Dulk 1985; E. D. Feigelson, L. Carkner & B. A. Wilking 1998; S. Kaur et al. 2024).

4.2 Spectral types and evolutionary classes

We searched for stellar spectral classifications associated with all detections by cross-matching with the catalogue of L. A. Hillenbrand et al. (2013), which contains spectral classifications for approximately 600 sources in the ONC. A search radius of 0.5 arcsec was adopted to account for significant proper motions and potential positional offsets between the radio sources and counterparts at other wavelengths. We note that positional coincidence does not necessarily imply physical association particularly in the case of multiple systems. Using these criteria 64 of our detected sources have reported spectral classifications.

Spectral classifications are available for only ∼28 per cent of the VLBA source population and therefore we do not attempt to draw conclusions about the spectral-type distribution of the full sample. Within the classified subsample, sources span a wide range of spectral types including M, K and K-M types. The highly variable sources with spectral classifications are likewise M, K and K-M types with two notable exceptions. ONC254 (spectral type O-B) which is a known multiple system (E. Lohsen 1976; M. Bossi et al. 1989; M. G. Petr et al. 1998) where the non-thermal radio emission is associated with a T Tauri companion (D. Schertl et al. 2003). ONC480 (spectral type B) which is discussed by S. A. Dzib et al. (2026b) as an astrometric binary and the non-thermal radio emission may similarly originate from a lower mass companion.

We also searched for protostellar evolutionary classes by cross-matching with the X-ray and near-infrared study of the inner ONC by L. Prisinzano et al. (2008) which provides evolutionary classes for X-ray detected YSOs. Using the same search parameters as for the spectral classifications we find 4 of our sources are classified as class II and 8 sources as class III. However, as noted by J. Forbrich et al. (2021), fewer than 5 per cent of the VLA sources from J. Forbrich et al. (2016) have counterparts in L. Prisinzano et al. (2008) and consequently, meaningful detection fractions for evolutionary classes cannot be derived. It should be noted that in Section 4.4 and Appendix B we additionally include details from other references in the discussion of higher variable sources where appropriate.

A powerful method for identifying YSOs is through association with X-ray sources using the COUP X-ray survey as a reference, as outlined in Section 1. We refer to J. Forbrich et al. (2016, 2021) and J. Vargas-González et al. (2021) who searched for COUP associations of the radio source positions used in this work, who also use a search radius of 0.5 arcsec. Of the 226 sources detected in this work 126 have COUP counterparts (∼56 per cent), and of these 36 of the VLBA radio sources are newly detected in this work identifying these YSOs as having a detectable non-thermal radio component. 100 VLBA radio sources (∼44 per cent) do not have COUP counterparts and of these 37 are newly detected VLBA sources.

Additionally, to identify sources as being associated with the ONC we cross-matched our source list with the *Hubble* Source Catalog (B. C. Whitmore et al. 2016) a master catalogue from archival HST imaging with the ACS, WFPC2 and WFC3 instruments. The VISTA near-infrared survey of the Orion A molecular cloud, called VISION, covering ∼18.3 square degrees reported by S. Meingast et al. (2016) was also cross-matched. Here we also used a search radius of 0.5 arcsec for both catalogues. There are 138 VLBA sources that have *Hubble* counterparts and 98 sources that have VISION counterparts, of these there are 40 sources that have *Hubble* and/or VISION counterparts that do not have COUP counterparts. For example, ONC476 (V∗ V2370 Ori) does not have a COUP counterpart but is coincident with a *Hubble* and VISION source within ∼0.2 arcsec and is classified by M. Fang et al. (2021) as an M5 star. There are 37 sources that lack any counterpart in the other catalogues (i.e. these sources are only detected in the radio). As a final check we compared source positions to a JWST image (NIRCAM general purpose F277W filter)[3] and found one association between our VLBA sources that lack any counterparts and a JWST source which is ONC551 at a separation of ∼0.2 arcsec.

We additionally cross-matched our VLBA source positions with the *Hubble* treasury program catalogue using the ACS/WFC of proplyds and circumstellar structures presented by L. Ricci, M. Robberto & D. R. Soderblom (2008), here we again use a search radius of 0.5 arcsec. We find 28 associations between our VLBA sources and sources within their catalogue, and find that 19 of these have COUP counterparts and 9 sources do not. These associations demonstrate that compact nonthermal radio emission is present in a number of systems associated with irradiated circumstellar structures in the ONC. It is important to highlight that the emission detected by the VLBA is distinct from the extended thermal emission associated with the ionized proplyd, which indicates a compact nonthermal component associated with the underlying YSO.

To assess whether these remaining sources lacking counterparts could be background sources we estimate the expected number of extragalactic sources based on the work by R. A. Windhorst et al. (1993), following the same methodology as J. Forbrich et al. (2021). We estimate up to 3 extragalactic radio sources at $S \geq 0.2$ mJy beam^{-1} (or 6.5σ of the average rms of the data) within the primary beam. However, if we instead consider the area that has been imaged in this work (i.e. the larger image sizes and the 575 phase centres which correspond to 9200 square arcsec) we estimate ∼0.2 background sources. It is also worth highlighting that this is based on VLA data and as VLBI observations are only sensitive to nonthermal emission this estimate represents an upper limit. Therefore, background contamination is considered negligible and most of these sources are likely members of the ONC. This is also consistent with the estimates and conclusion of J. Forbrich et al. (2021).

4.3 Radio variability

Variability was quantified using the VF as defined in Section 3.1, derived from *per-epoch* peak flux densities. We identify 21 higher

[3] https://jwst.esac.esa.int/archive/

Downloaded from academic.oup.com/mnras/article/552/4/stag1806/8834038 by guest on 23 October 2026

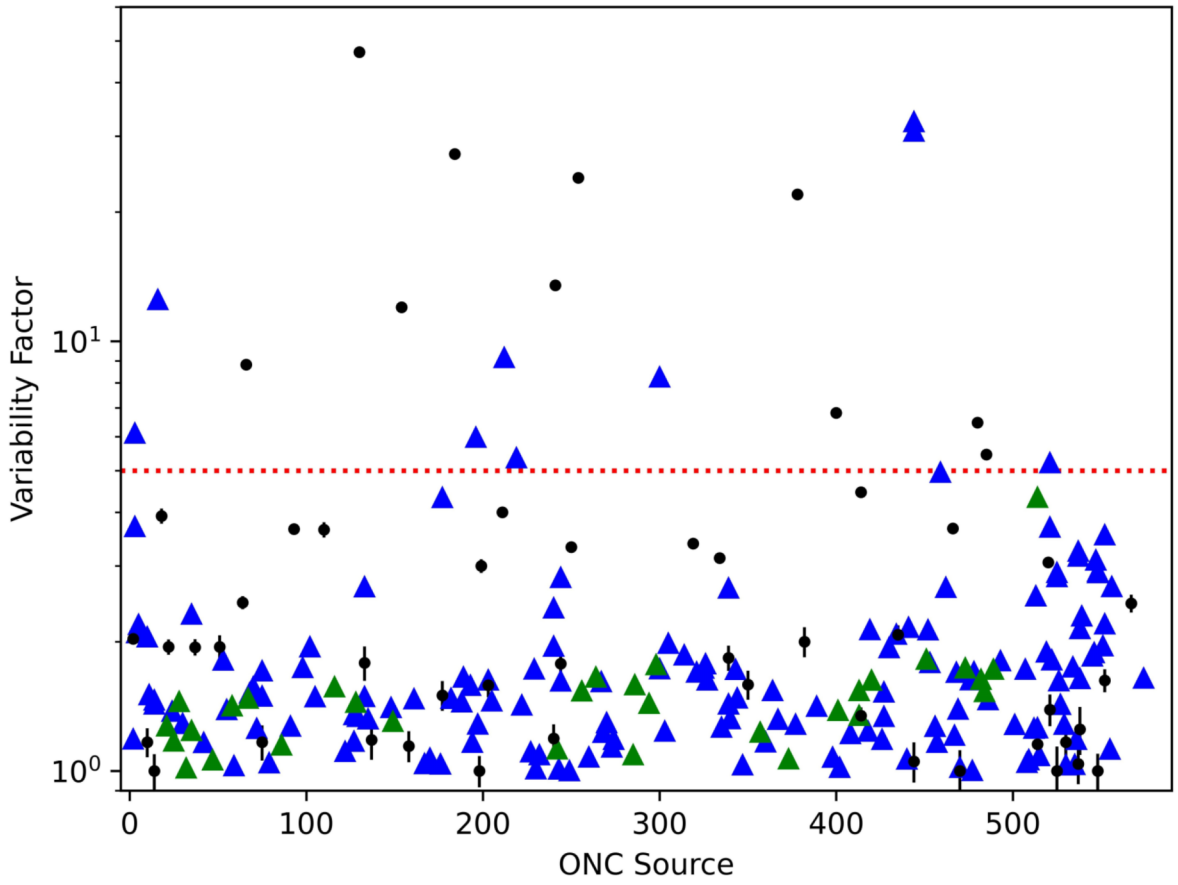


Figure 3. A plot of all variability factors from the eight epochs of VLBA data. Variability factors represent the ratio between the highest and lowest flux densities where higher numbers indicate increased variability. Sources that are detected in multiple epochs enable the variability factor to be calculated directly (black points). On the other hand, for sources that are only detected in a single epoch a lower limit for the variability factor was calculated using the 5.5σ value of the lowest rms noise as an upper limit (blue triangles for single detections in the normal data and green for the concatenated data). The red dotted line marks the limit for higher variability of VF $\geq$ 5 (see Section 3.1).

variable sources (∼9 per cent of unique sources) where 11 sources have measured VFs $\geq$ 5 and a further 10 sources have lower limits $\geq$ 5. We also highlight that 4 sources (∼2 per cent) exhibit extreme variability with VF $\geq$ 15, these are discussed in Section 4.4. Table 2 lists the flux densities, COUP numbers and inter-epoch VFs. Table 3 lists additional source information: signal-to-noise, source positions, separation from nominal VLA position, YSO class and spectral type. Table 4 lists the COUP numbers, flux densities and VFs for sources detected only in the concatenated data. The sources exhibiting higher VFs all have COUP counterparts identifying them as YSOs and some have YSO evolutionary classes (see Section 4.4 and Appendix B).

Fig. 3 displays the maximum VF for sources detected more than once (black points), lower limits for sources detected in only a single epoch (blue triangles) and lower limits for sources detected solely in the concatenated data (green triangles). The red dotted line indicates the threshold of higher variability of VF = 5. Sources lying on this threshold are classified as highly variable if their uncertainty overlaps VF = 5 or when they are constrained by lower limits. For example, ONC414.1 has a VF = 4.5 ± 0.6 and is therefore consistent with VF $\geq$ 5 within uncertainties. We note, as discussed in Section 3.1, that all variability factors derived in this work are significant with S/N $\geq$ 3. Additionally, we examined distributions of VFs for the 54 total sources with directly derived VFs to search for evidence of breaks or bimodal structure. No clear evidence for either is apparent, although the relatively small number of sources limits the sensitivity of this test.

Several sources previously reported as radio-variable are detected in our data but do not exhibit high variability over the epochs sampled here. These include the 'ORBS' source (ONC198) reported by J. Forbrich, K. M. Menten & M. J. Reid (2008) and sources ONC053 (COUP 427), ONC110 (COUP 530), ONC469 (COUP 1101) and θ^2 Ori A (ONC515 or COUP 1232) reported by J. Forbrich et al. (2017). J. Vargas-González (2024) discuss sources ONC022, 326, 435, 547 and 557 being detected at higher signal-to-noise within their VLA data. Of these ONC022 and 557 have VFs $\geq$ 5 in their work and were not classified as variable by J. Forbrich et al. (2017).

These sources being detected in our VLBA data enable their VFs to be evaluated within the framework of this study. All of these sources mentioned above have VFs $<$ 5. These variability factors when compared to earlier reports of high variability underscore the importance of multi-epoch observations for characterizing intermittent radio emission as well as the need for closely spaced epochs to probe shorter time-scales.

Additionally, we report the second VLBI detection of the variable source θ^1 Ori C (ONC305) in the eighth epoch at a peak flux density of 0.24 ± 0.02 mJy beam^{-1} (S/N = 12.3). This source is

Downloaded from academic.oup.com/mnras/article/552/4/stag1806/8834038 by guest on 23 October 2026

Table 4. Table of flux density measurements for the concatenated data in mJy beam^{-1} from the resulting `imfit` (CASA Team 2022) and the inter-epoch variability factors for each concatenated VLBA data epoch: BF123AB, BF131AB, BF131CD. Variability factors that are listed as being more than (>) are single detected sources and represent lower limits.

[FRM2016]	COUP	BF123AB	BF131AB	BF131CD	Variability factor
021	343	0.13 ± 0.01	-	-	>1.3
025	-	0.10 ± 0.01	-	-	>1.0
028	358	-	-	0.12 ± 0.01	>1.4
032	378	0.11 ± 0.01	-	-	>1.0
035	390	0.10 ± 0.01	-	-	>1.0
047	-	0.08 ± 0.01	-	-	>1.0
058	-	-	-	0.12 ± 0.01	>1.4
067	-	-	0.13 ± 0.01	-	>1.5
086	-	0.12 ± 0.01	-	-	>1.1
116	-	-	-	0.13 ± 0.02	>1.6
128	-	-	0.12 ± 0.01	-	>1.4
149	-	0.14 ± 0.01	-	-	>1.3
203[a]	655	0.12 ± 0.01	-	-	1.6 ± 0.2
242	723	0.09 ± 0.01	-	-	>1.0
256	747	-	0.13 ± 0.01	-	>1.5
264	758	-	0.14 ± 0.01	-	>1.7
285	783	0.12 ± 0.01	-	-	>1.1
286	789	-	0.14 ± 0.02	-	>1.6
294	799	-	0.12 ± 0.02	-	>1.4
298	-	-	-	0.15 ± 0.02	>1.8
357	896	0.13 ± 0.01	-	-	>1.2
373	-	0.08 ± 0.01	-	-	>1.0
401	964	-	-	0.12 ± 0.02	>1.4
413.1	-	-	0.13 ± 0.02	-	>1.5
413.2	-	-	0.12 ± 0.01	-	>1.3
420	-	-	0.14 ± 0.02	-	>1.6
451	-	-	0.16 ± 0.02	-	>1.8
470[a]	-	-	0.12 ± 0.01	-	1.0 ± 0.1
473	1107	-	-	0.15 ± 0.01	>1.7
482	-	-	-	0.14 ± 0.01	>1.6
484	-	-	-	0.13 ± 0.01	>1.5
489	1143	-	-	0.15 ± 0.01	>1.7
514[a]	-	-	0.13 ± 0.01	-	1.2 ± 0.1
530[a]	1289	-	0.14 ± 0.02	-	1.2 ± 0.1

[a]These sources are detected in the normal and concatenated data which then allows the variability factor to be derived.

only detected in one out of the eight epochs analysed here indicating an intermittent source. The first VLBI detection of this source is reported by S. A. Dzib et al. (2026a), where they report the radio detection at a separation of 14 mas (∼5 AU) from the optical source. This source has a known companion with an orbital period of 11.26 ± 0.05 yr and semimajor axis of 44 ± 3 mas reported by S. Kraus et al. (2009). The companion has a mass estimate of ∼11 $M_\odot$ (Y. Y. Balega et al. 2014) which is well above the expected mass range for magnetically active young stars. S. A. Dzib et al. (2026a) discuss that considering the orbital configuration reported by S. Kraus et al. (2009) that the radio emission is likely associated with the companion. However, additional VLBI observations are required to study and confirm the nature of this source.

We also report a single VLBI detection of source ONC441 in the seventh epoch at a flux density of 0.29 ± 0.02 mJy beam^{-1} (S/N = 12.2), with a lower limit of the VF of > 2.2. This source was reported as a radio source by J. Forbrich et al. (2016) and has previously been identified as a radio counterpart to a component of a proposed Jupiter Mass Binary Object (JuMBO) by L. F. Rodríguez, L. Loinard & L. A. Zapata (2024). These authors find a persistent VLA counterpart across multiple observations. Our detection provides evidence that the source also produces nonthermal radio emission. Although the nature of this source remains unclear, near-infrared analysis by K. L. Luhman (2024) indicates that this source is a close pair of low-mass stars.

4.4 Highest variability factors

In this section we discuss the sources exhibiting the most extreme variability factors; here we highlight sources with VFs ≥ 15 to illustrate the highest VFs in this study which totals four sources. Additional highly variable sources are described in Appendix B. Fig. 4 shows continuum images for the four sources discussed below showing their maximum and minimum flux densities.

4.4.1 ONC130 (COUP 554 or 2MASS J05351356-0523552)

ONC130 is classified as a YSO with a disc by S. T. Megeath et al. (2012) from their *Spitzer* mid-infrared observations, and as a class I YSO by J. E. Großschedl et al. (2019) using near-infrared data from the ESO-VISTA Orion A survey (VISION). Fig. 5 shows the light curve of ONC130 (upper left panel), presenting the per-epoch peak flux densities and upper limits (red arrows) for epochs with non-detections. The light curve shows a significant increase in the flux density in the first four epochs peaking in the fourth which are separated by various time-scales as seen by the epoch

Downloaded from academic.oup.com/mnras/article/552/4/stag1806/8834038 by guest on 23 October 2026

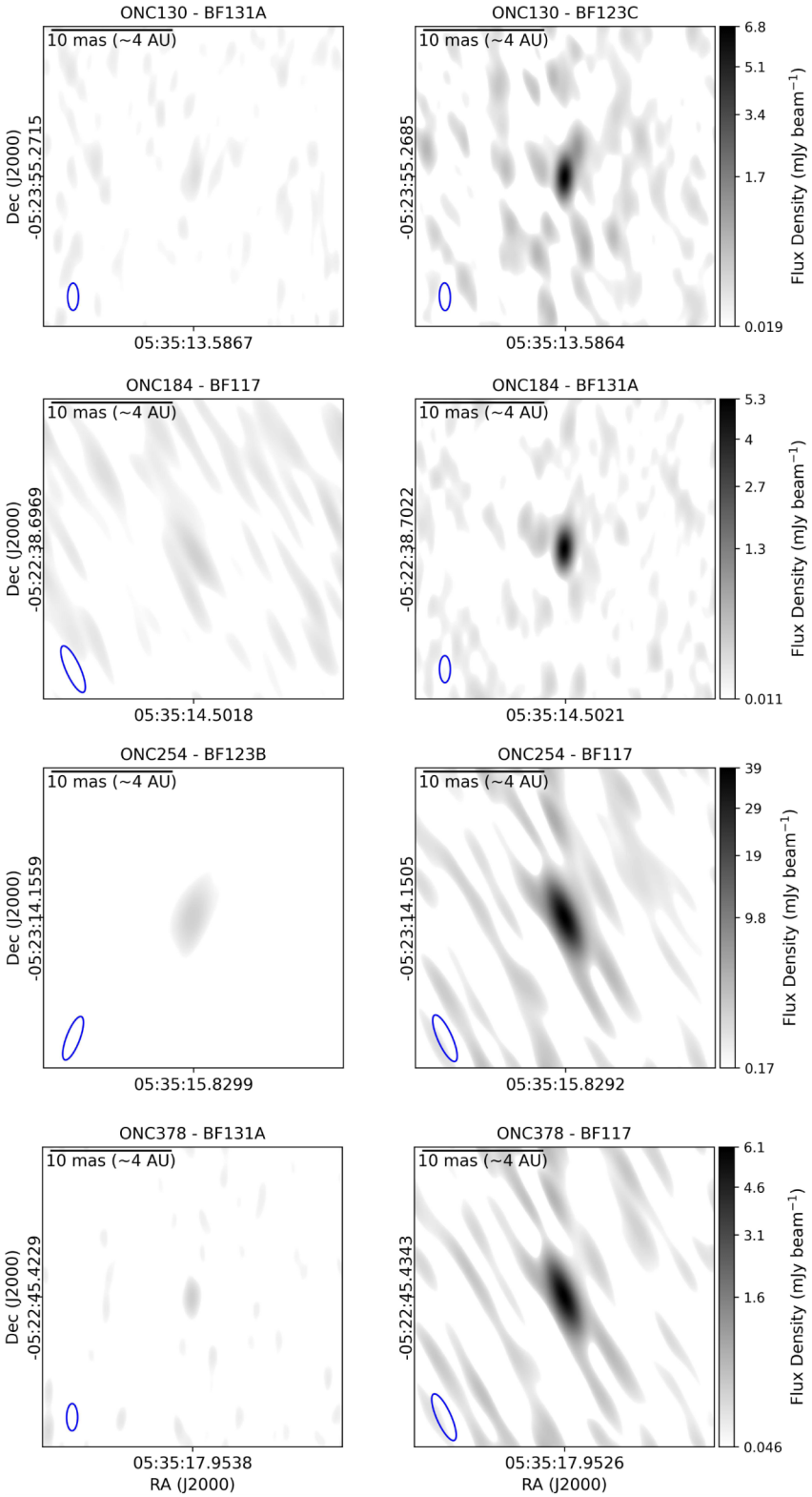


Figure 4. Grid plot of radio continuum images showing the four sources with VF $\geq$ 15. The RA and Decl. of the centre of the image are shown, in the bottom left of each image is the synthesized beam and upper left is a scale bar (10 mas corresponds to ~4 AU at the distance of the ONC). The images are 512 $\times$ 512 in size with a pixel size of 0.05 mas to highlight the source. A colourbar is to the right of each row showing flux density in mJy beam^{-1} illustrating the range associated with these highly variable source detections.

Downloaded from academic.oup.com/mnras/article/552/4/stag1806/8834038 by guest on 23 October 2026

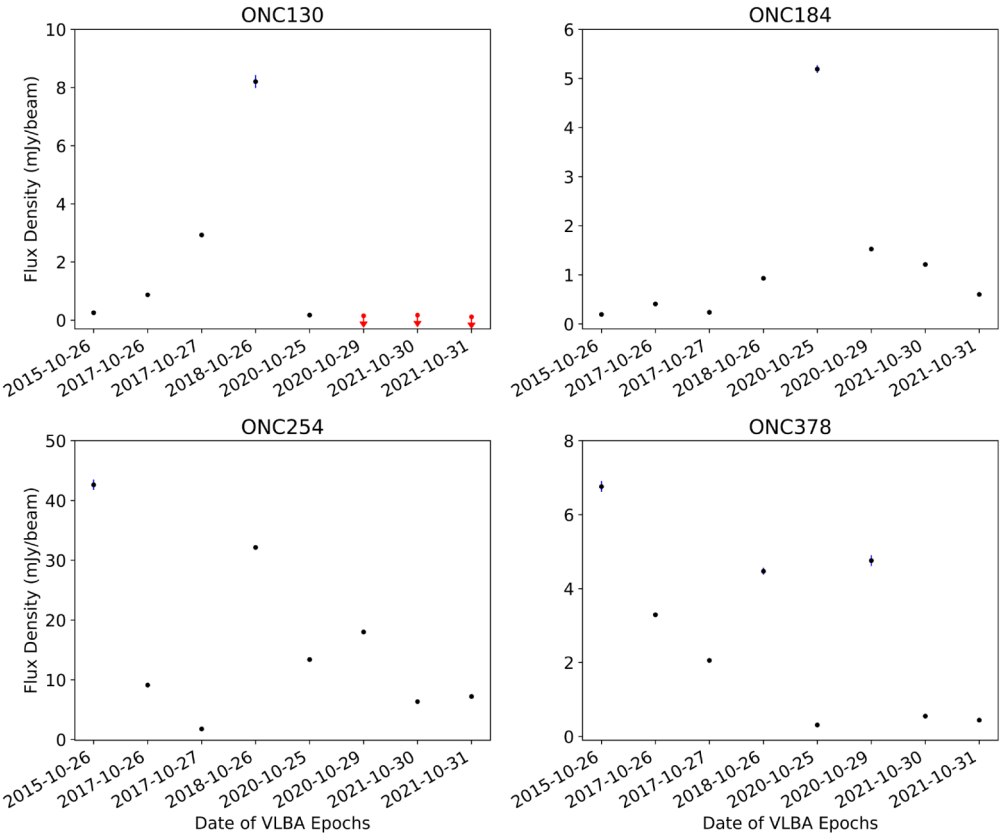


Figure 5. Light curves for the four sources with the highest VFs using the peak per-epoch flux density. The dates of each epoch are shown along with the per-epoch peak flux density. Here, if a source is not detected in an epoch, we show upper limits as red arrows.

dates at the bottom of the light curve. This source is detected in a total of five epochs with a highest flux density of 8.20 ± 0.22 mJy beam^{-1} in the fourth epoch and a lowest in the fifth epoch of 0.18 ± 0.02 mJy beam^{-1}. This corresponds to VF $= 47.1 \pm 6.4$ which is the highest observed in our data.

4.4.2 ONC184 (COUP 639 or ALMA J053514.5010-052238.674)

ONC184 is classified as a variable YSO based on observations from the Gould's Belt VLA Survey Program (S. A. Dzib et al. 2013), and M. Kounkel et al. (2014) report a variability percentage of 60.7±16.1. Additionally, K. V. Getman et al. (2005) and V. M. Rivilla et al. (2015) discuss this source as a flaring object in X-ray and radio, respectively. The light curve for this source is shown in the upper right panel of Fig. 5 and exhibits a pronounced increase in flux density during the fifth epoch. ONC184 is detected in all VLBA epochs with a highest epoch-average peak flux density of 5.19 ± 0.08 mJy beam^{-1} in the fifth epoch, and a lowest peak flux density of 0.19 ± 0.02 mJy beam^{-1} in the first epoch. This corresponds to VF $= 27.3 \pm 2.9$.

4.4.3 ONC254 (COUP 745 or θ^1Ori A_2)

ONC254 is a member of the well-studied multiple system θ^1Ori A. The primary component (θ^1Ori A_1) has a spectral type B0.5 as reported by H. Levato & H. A. Abt (1976) from their Kitt Peak 0.9 m Cassegrain spectrograph observations. It has mass estimates of 18.91 $M_\odot$ by L. A. Hillenbrand (1997), 20 $M_\odot$ from the SAO 6 m telescope data reported by G. Weigelt et al. (1999), and $14 \pm 5 M_\odot$ by S. Simón-Díaz et al. (2006) from their Isaac Newton 2.5 m Telescope (INT) data. E. Lohsen (1976) reports an eclipsing binary with a period of 65.43 d from Bochum 0.61 m telescope observations, and H. A. Abt, R. Wang & O. Cardona (1991) derived a period of 65.09 ± 0.07 d using the 2.1 m Cassegrain spectrograph. This tight companion is θ^1Ori A_3 and M. Bossi et al. (1989) report from the thermal spectrum that this companion is at a separation of 0.71 AU and is a T Tauri star with a mass of 2.5-2.7 $M_\odot$.

M. G. Petr et al. (1998) identify another companion (θ^1Ori A_2) at a separation of ∼200 mas (corresponding to ∼80 AU at the distance of the ONC), and they speculate that the radio emission is likely from this companion. This was confirmed by S. A. Dzib et al. (2021) through a comparison of VLBA and *Gaia* astrometry for associated sources. The mass of θ^1Ori A_2 is reported by D. Schertl et al. (2003) as 4 $M_\odot$ with a period of 214 yr orbiting the tight binary θ^1Ori A_1+θ^1 Ori A_3, from their SAO 6 m telescope observations. GRAVITY Collaboration (2018) confirmed this third companion is gravitationally bound to the system from their observations using the GRAVITY instrument at the Very Large Telescope Interferometer.

θ^1Ori A_2 is detected in all eight epochs and exhibits strong variability. The light curve of this source is shown in the lower left panel of Fig. 5 and shows considerable variability across epochs. The highest epoch-averaged peak flux density is 42.62 ± 0.87 mJy beam^{-1} in the first epoch, and lowest of 1.77 ± 0.04 mJy beam^{-1} in the third epoch. This corresponds to VF $= 24.0 \pm 0.7$. Interestingly, this source exhibits lower but still high variability of VF $= 5.2 \pm 0.1$ on a time-scale of just 1 d. The extreme variability observed across different time-scales suggests

Downloaded from academic.oup.com/mnras/article/552/4/stag1806/8834038 by guest on 23 October 2026

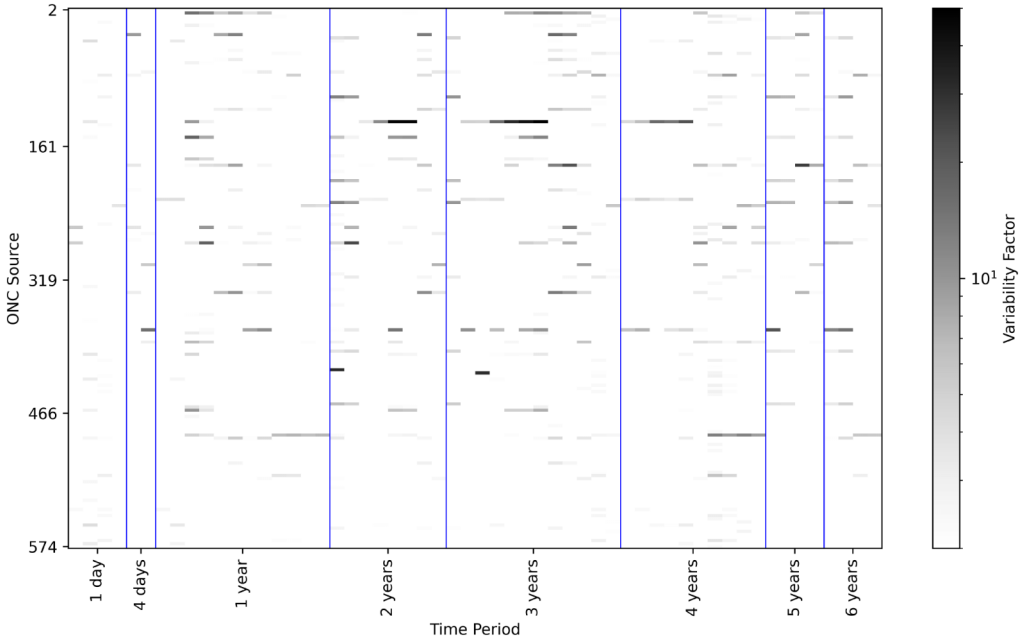


Figure 6. A heatmap showing the VFs ≥ 2 per source that are separated into time-scales. The *y*-axis indicates the source identifier. The columns are sorted into the respective time periods between epochs, and the vertical blue lines indicate the boundaries of each time period. The highest derived VF is associated with ONC130 at VF $= 47.1 \pm 6.4$.

variability on shorter time-scales but is difficult to characterize due to the complexity of this source.

4.4.4 ONC378 (COUP 932 or MT Ori)

ONC378 is detected in all epochs. It is classified by L. A. Hillenbrand et al. (2013) as spectral type G-K3. Mass estimates for this source vary across the literature: L. Wei et al. (2024) obtain a mass of $0.387 \pm 0.022\ M_{\odot}$ using the 'MIST' stellar evolutionary model from their near-infrared 'NIRSPEC' work from Keck II 10 m telescope observations (J. Choi et al. 2016; A. Dotter 2016). Whereas, K. V. Getman & E. D. Feigelson (2021, see their appendix C) give a mass of $3.7\ M_{\odot}$ from their *Chandra* data, which is also discussed by K. V. Getman et al. (2022).

The light curve for this source is shown in the lower right panel of Fig. 5 and displays considerable variability in the per-epoch peak flux densities. The highest peak flux density is 6.76 ± 0.15 mJy beam^{-1} in the first epoch while the lowest of 0.31 ± 0.02 mJy beam^{-1} is in the fifth epoch. This corresponds to VF $= 22.0 \pm 1.5$. Interestingly, this source exhibits high variability on a shorter time-scale of 4 d of VF $= 15.3 \pm 1.1$. As discussed in Section 4.5 this source exhibits a range of variability across different time-scales with markedly different extremes measured for the same object.

4.5 Source and variability occurrence

Multi-epoch observations enable the characterization of radio variability across a wide range of time-scales, and the intermittent nature of non-thermal radio emission makes such an approach essential. By using per-epoch peak flux densities we probe variability on time-scales ranging from several years to 1 d (see Table 1 for epoch dates).

Fig. 6 shows the variability factors that are higher than 2 for all sources at all available time separations between epochs as a heatmap, which highlights not only the highest variability but also where source's fluxes vary by at least a factor of 2. The 11 most variable sources (VFs ≥ 5) that have multiple detections exhibit a variety of VFs across the different time-scales between epochs. For example, ONC130 has a maximum VF of 47.1 ± 6.4 on a time-scale of 2 yr, compared to 9.4 ± 0.3 on a 1 yr time-scale and 3.4 ± 0.1 on 1 d. Similarly, ONC241 exhibits a highest VF of 13.8 ± 1.4 on a time-scale of 3 yr, while the second highest VF is 9.8 ± 1.0 on a time-scale of just 1 d.

The presence of such a broad range of variability factors for individual sources across differing time-scales, as illustrated in Fig. 6, indicates a substantial fraction of the radio variability likely occurs on time-scales shorter than those sampled in this work. This would also be consistent with previous studies of flaring associated with YSOs at higher time resolutions. For example, G. C. Bower et al. (2003) report a bright YSO millimetre flare (GMR-A or ONC066) in the ONC on a time-scale of several hours and J. Forbrich et al. (2008) report the first bright flare observed at centimetre wavelengths (the 'ORBS' source or ONC198) on a time-scale of several hours. J. Forbrich et al. (2017) then report several flares occurring on time-scales from hours down to $\sim$30 min. Additionally, J. Vargas-González (2024) reports variability at millimetre wavelengths for several sources and for two sources (ONC098 and 130) from the first four epochs of the VLBA data used in this work, both on time-scales of hours.

We now investigate the detectability and variability of YSOs across the eight epochs of this work with the aim of quantifying how often these sources are detected and how the radio emission varies between epochs. We consider the 254 sources with COUP counterparts that lie within the adopted search radius of their respective phase centre to take a conservative approach that ensures these are YSOs (see discussions in Sections 1 and 4). There is additional evidence that sources without X-ray counterparts are associated with YSOs and a discussion of all sources in the context of their identification as ONC members is in Section 4.2; therefore, the approach taken here results in a lower limit.

Downloaded from academic.oup.com/mnras/article/552/4/stag1806/8834038 by guest on 23 October 2026

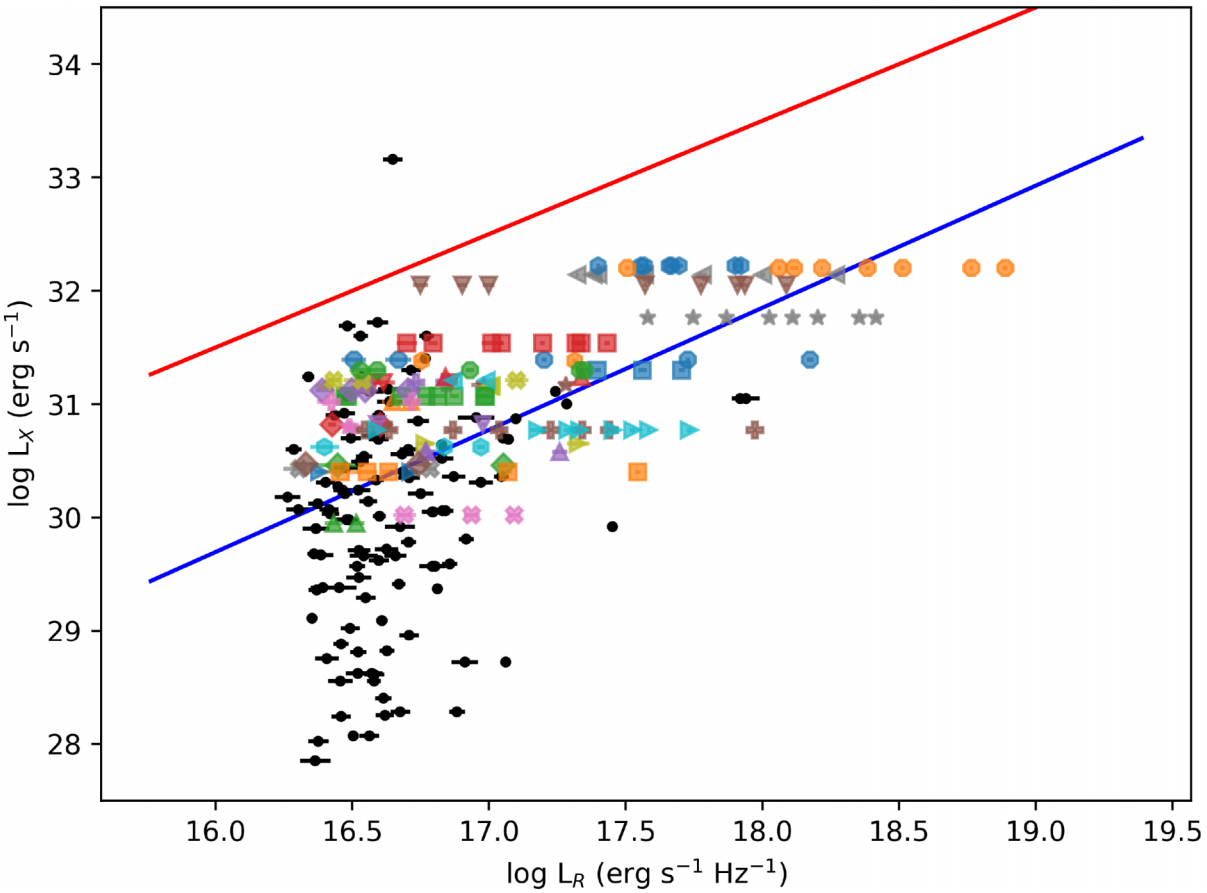


Figure 7. X-ray luminosities as a function of radio luminosity for VLBA detections and associated COUP counterparts (K. V. Getman et al. 2005). There are 126 VLBA sources that have COUP counterparts, some are detected multiple times totalling 250 detections. Black points are sources detected once and the coloured points with different markers indicate a source detected more than once. This shows the range of radio luminosity measurements for these sources. The blue line is the fit for our data and the red line is the original Güdel–Benz relation. The uncertainties in the luminosities are the error propagation of the flux densities and the error in the fit is the error propagation of the luminosities.

Of the 254 sources considered here 126 are detected within our VLBA data totalling 250 detections across all eight epochs.

The probability of detecting a YSO in a given epoch can be estimated from the total number of detections divided by the total number of sources with COUP counterparts and the number of epochs, $\rho = 250/(254 \times 8) \approx 12$ per cent. This indicates that ∼12 per cent are detected in any individual epoch. In addition, there are 92 sources that are detected only once. Considering these together highlights that YSO radio emission is highly intermittent.

To assess how long this emission persists we consider detections in adjacent epochs, where adjacent epochs means all subsequent epochs (e.g. the first and second epoch are adjacent and separated by 2 yr, as seen in Table 1). There are 25 sources detected in adjacent epochs and of these 19 sources are detected in closely spaced epochs (closely spaced epochs are separated by 1 or 4 d) which corresponds to a probability of ∼9 per cent. The relative rarity of detections across closely spaced epochs suggests that higher variability is occurring on time-scales shorter than the shortest spacing between epochs.

We now consider the occurrence of higher variability defined as VF ≥ 5, where we find 21 sources which corresponds to ∼8 per cent of VLBA-detected sources. Of these, 12 sources exhibit VF ≥ 5 between adjacent epochs, indicating that ∼5 per cent of the source sample shows high variability between adjacent epochs, which also corresponds to ∼57 per cent of the subsample of higher variable sources.

Finally, we investigate closely spaced epochs (separated by 1 or 4 d). Of the 21 sources that are considered highly variable 3 sources (ONC241, 254, and 378, which are all associated with YSO sources; see Section 4.4 and Appendix B) have VFs ≥ 5 between these closely spaced epochs (∼14 per cent of the subsample of highly variable sources). These cases demonstrate that large amplitude variability can occur over the shortest epoch spacing of 1 d.

Considering these results together shows that YSO radio emission is both highly intermittent and strongly variable. The low probability of detecting a source in a given epoch combined with the low likelihood of detections in closely spaced epochs further suggests that YSO variability is likely occurring on time-scales shorter than our shortest epoch spacing of 1 d.

4.6 Radio-X-ray connection

The non-thermal gyrosynchrotron radio emission in YSOs originates from mildly relativistic electrons associated with coronal-type activity. Thermal bremsstrahlung X-ray emission occurs from heated plasma within the corona (G. A. Dulk 1985; E. D. Feigelson & T. Montmerle 1999; M. Güdel 2002; J. Forbrich & S. J.

Downloaded from academic.oup.com/mnras/article/552/4/stag1806/8834038 by guest on 23 October 2026

Wolk 2013). There is an empirical relation between non-thermal radio and thermal X-ray emission first studied for coronally active stars by M. Guedel & A. O. Benz (1993) and A. O. Benz & M. Guedel (1994), the 'Güdel–Benz (G-B) relation'.

This relation has previously been studied for the ONC using VLA and COUP data by J. Forbrich & S. J. Wolk (2013) and by V. Yanza et al. (2022) who also used VLA and COUP data but additionally used the VLBA source detections from J. Forbrich et al. (2021) as a selection criterion of their VLA sources. These studies were somewhat limited as it is difficult to disentangle thermal and non-thermal emission within VLA observations (see Section 1). However, these studies both found that their data are compatible with the relation. We therefore investigate this using VLBA data that provides the unique perspective of being sensitive exclusively to non-thermal emission.

Here we use the COUP X-ray luminosities as the COUP catalogue is the most sensitive X-ray survey of the ONC and this high sensitivity allows the spectral fitting required to derive total band (0.5–8 keV) absorption-corrected luminosities which are corrected for interstellar absorption as discussed by K. V. Getman et al. (2005). We then derived radio luminosities from our multi-epoch VLBA data. We highlight that these data sets are not simultaneous and therefore variability in one data set would not be observed in the other; this methodology of using non-simultaneous data is also extensively discussed by J. Forbrich & S. J. Wolk (2013). The empirical correlation reported by M. Guedel & A. O. Benz (1993) and A. O. Benz & M. Guedel (1994) is

$$\frac{L_X}{L_R} = k \cdot 10^{15.5\pm0.5}, \tag{2}$$

where $k \leq 1$ accounts for different types of stars. A. O. Benz & M. Guedel (1994) give $k \approx 0.17$ for RS CVn binaries, Algol systems, FK Com stars, and Post T Tauri stars. However, for YSOs other studies have shown that k is significantly less than 1. For example, S. A. Dzib et al. (2015) give $k = 0.03$ for YSOs of several star-forming regions.

There are 126 of our VLBA sources that have COUP counterparts totalling 250 detections, so we use the luminosities for these sources. We also correct the X-ray luminosities to the distance used in this work as K. V. Getman et al. (2005) used an estimate of 450 pc. We then use a linear least-squares fit in log-log space, corresponding to a power-law scaling between radio and X-ray luminosities, to our 250 total detections which gives $\log L_X = (12.5 \pm 1.6) + (1.08 \pm 0.10) \log L_R$ with a Pearson correlation coefficient (R) of 0.58. The Pearson coefficient of 0.58 indicates a moderate positive correlation, which is statistically significant ($p < 0.001$). Despite the significant association, the moderate magnitude of the correlation indicates considerable scatter in the data, which is at least partly due to radio and X-ray variability. This result improves upon previous studies from the unique perspective enabled by VLBA data and shows a positive correlation agreeing with the previous work by J. Forbrich & S. J. Wolk (2013) and V. Yanza et al. (2022).

Fig. 7 shows the X-ray luminosities as a function of the radio luminosities we derived. Sources detected in multiple VLBA epochs are plotted individually using unique markers and colours, and sources detected once are indicated by black markers. This highlights the variability seen in the radio sources. The red line is the original G-B relation and the blue line is our fit. The formal luminosity uncertainties are derived from the propagated flux density errors and the fit uncertainty is the propagated luminosity errors.

Our fit lies roughly two orders of magnitude below the original G-B relation in X-ray luminosities. This has been observed by the other ONC studies previously mentioned, J. Forbrich & S. J. Wolk (2013) and V. Yanza et al. (2022), who both found their sources are under-luminous in X-ray (or 'radio-bright') compared to the original G-B relation. It should be noted that the work presented by V. Yanza et al. (2022) is focused on the M17 nebula but they also investigate this for the ONC. The theoretical YSO modelling work conducted by C. O. G. Waterfall et al. (2019) also agrees with our results. Their model uses a magnetic flux tube filled with non-thermal electrons and their results show a departure from the G-B relation in a similar manner to our results.

The systematic offset from the original G-B relation indicates that the YSO population occupies a different normalization. Such offsets are not unexpected for young stars which are highly active and where the radio and X-ray relation is known to differ from magnetically active main-sequence stars (e.g. M. Guedel & A. O. Benz 1993; J. Forbrich & S. J. Wolk 2013). In particular, for highly active stars the X-ray emission can reach a saturation level in $L_X/L_{\rm bol}$ whereas nonthermal radio emission associated with accelerated electrons need not saturate in the same manner (e.g. M. Güdel 2004). This can result in relatively enhanced radio emission and therefore a departure from the canonical G-B relation. The different magnetic and coronal environments of young stars, together with their high levels of magnetic activity, could contribute to the population-dependent normalization. Similarly, J. Forbrich & S. J. Wolk (2013) found that nonthermal radio sources and saturated X-ray sources within the ONC are usually closer to the G-B relation but with systematically higher radio luminosities. Additionally, the strong variability of the radio and X-ray emission, combined with the non-simultaneity of the observations, is expected to introduce scatter reducing the statistical significance of the observed offset.

The slope in our fit is consistent with unity within the uncertainties, which indicates a nearly linear relation between L_X and L_R. In this case the relation can be written approximately in the form of the G-B relation. We can write our fit in the linear form as $L_X/L_R = 10^{12.5\pm1.6} L_R^{0.08\pm0.10}$. Comparing this expression with the G-B relation (equation 2), we obtain

$$k = 10^{-3.0} L_R^{0.08}. \tag{3}$$

Because the fitted slope is consistent with unity, k depends only weakly on L_R. For representative radio luminosities in our sample ($L_R \sim 10^{16}$–10^{19} erg s^{-1} Hz^{-1}), we obtain k ranging from 0.02 to 0.03, in agreement with the empirical value of $k = 0.03$ reported by S. A. Dzib et al. (2015).

5 SUMMARY AND CONCLUSIONS

We present an updated non-thermal census of the ONC, building upon previous VLBA studies by J. Forbrich et al. (2021) and S. A. Dzib et al. (2021). We extend this work with a per-epoch variability analysis. This is based on four more VLBA epochs of follow-up observations of the 575 VLA radio sources, totalling eight VLBA epochs each ∼7 h in duration obtained between 2015 and 2021.

The primary goals of this work are to update the non-thermal detection statistics and obtain per-epoch photometry to characterize variability statistics. By measuring epoch-averaged peak flux densities we investigate variability on time-scales down to 1 d. We find 21 sources that exhibit high variability (VF ≥ 5) and that significant variability (where a VF has an S/N ≥ 3) is common. The diversity of the observed variability indicates

Downloaded from academic.oup.com/mnras/article/552/4/stag1806/8834038 by guest on 23 October 2026

that it is likely occurring on time-scales even shorter than our shortest epoch spacing of 1 d. This is consistent with previous studies, for example, J. Forbrich et al. (2017) found three sources at centimetre wavelengths exhibiting extreme variability on time-scales between 0.4 and 0.7 h and J. Vargas-González (2024) reports variability for two sources at high time resolution on the order of hours. The main results and conclusions can be summarized as follows:

(i) We present updated non-thermal detection statistics extending the work of J. Forbrich et al. (2021) by adding four new epochs and analysing detections across all eight epochs. Of the 575 VLA targets we detect 226 unique sources (335 total detections) corresponding to an overall detection fraction of 39 per cent. Although it is known that some targets are non-stellar in origin and therefore are not expected to be detected by VLBA observations. The majority of the sources appear in only a single epoch (188 sources or ∼83 per cent), while 35 sources (∼16 per cent of unique sources) are detected in more than one epoch and of these there are 9 sources (∼4 per cent of unique sources) that are detected in all eight epochs. We report the detection of 93 new sources (∼41 per cent of unique sources) that were not detected in the first four epochs reported by J. Forbrich et al. (2021). The predominance of single-epoch detections, where we detect a source that is then not detected in subsequent epochs, underlines the highly intermittent nature of the non-thermal source population. Additionally, no significant circularly polarized emission (Stokes V) is detected for any source. We estimate upper limits on the circular polarization fraction that span a wide range of ∼1 to 100 per cent with a median of ∼13 per cent.

(ii) Non-detections in the VLBA data cannot be explained solely by the difference in sensitivity between the VLBA (average rms of 35 μJy beam^{-1}) and the VLA (nominal rms of 3 μJy beam^{-1}). The absence of VLBA counterparts for a subset of VLA sources could partially be explained by variability but is also consistent with sources lacking a compact non-thermal emission component.

(iii) Source variability was quantified using the VF derived from *per-epoch* peak flux densities. All derived VFs in this work are considered significant with S/N ≥ 3. Of the 226 unique sources 21 (∼9 per cent of unique sources) exhibit high variability (VF ≥ 5), including 8 sources (∼4 per cent) showing extreme variability with VF ≥ 10. The most variable source in the sample is associated with the class I YSO source ONC130 with a VF of 47.1 ± 6.4. Significant variability is observed at multiple time-scales and in some cases for the same source. The differing VF values at different time-scales for individual sources is consistent with variability occurring on time-scales shorter than our shortest spacing between epochs of 1 d.

(iv) Cross-matching our VLBA detections with the spectral classifications from L. A. Hillenbrand et al. (2013) reveals that there are 64 sources that have spectral classifications within our sample. These are mostly M, K and K-M classes, however, it should be highlighted that this only represents ∼28 per cent of the VLBA source population.

(v) We also cross-matched our VLBA detections with the COUP X-ray survey (K. V. Getman et al. 2005) with the main motivation being to identify these sources as YSOs as elevated X-ray emission in this context is associated with pre-main-sequence stars. We find 126 of the 226 unique radio sources (∼56 per cent) as having X-ray counterparts. We also cross-match with *Hubble* (B. C. Whitmore et al. 2016) and VISION (S. Meingast et al. 2016) catalogues where we find 138 and 98 associations, respectively. There are 36 remaining sources that lack any counterparts. We then estimate the number of background sources within the VLBA primary beam as up to 3 sources and within the imaged area by this work as ∼0.2 sources. Therefore, the contribution from background sources is considered negligible and the sources lacking any counterparts are likely ONC members. We also identify 36 newly detected sources that have COUP counterparts confirming these YSOs as having an observable non-thermal radio component and 37 new VLBA detections that do not have COUP counterparts.

(vi) Investigating the G-B relation, we find that the VLBA-detected sources are systematically under-luminous in X-rays relative to the original relation. The offset may be a result of the radio and X-ray observations being non-simultaneous as discussed by J. Forbrich & S. J. Wolk (2013). Despite this offset we find a moderate positive correlation between radio and X-ray luminosities with a positive Pearson correlation coefficient of (R) = 0.58. This is a novel measurement as VLBA observations means the sources are known to be non-thermal and the G-B relation is thought to only hold for non-thermal emission. However, previous work used VLA observations that include both thermal and non-thermal emission (e.g. J. Forbrich & S. J. Wolk 2013; V. Yanza et al. 2022).

(vii) We estimate the detectability and variability of YSOs across the eight epochs of this work. Of the 575 targets of this work there are 254 that have COUP counterparts. Of these there are 126 detected in our VLBA epochs totalling 250 detections (as some are detected multiple times). The probability of detecting a YSO in a given epoch is estimated as ∼12 per cent, further highlighting that YSOs are highly intermittent. We then considered detections in closely spaced epochs to assess the persistence of radio emission (closely spaced epochs are separated by 1 or 4 d), where we find 19 sources corresponding to a probability of ∼9 per cent, showing that emission rarely persists across epochs. We considered the occurrence of higher variability where we find 21 sources (∼8 per cent of detected sources) exhibiting higher variability, of these there are 12 sources (∼5 per cent) that exhibit higher variability between adjacent epochs. Finally, closely spaced epochs (separated by up to a few days) were investigated in the context of high variability where 3 sources exhibit higher variability across closely spaced epochs (∼14 per cent of highly variable sources). These results show that YSO radio emission is highly intermittent and variable, and the low probabilities of detecting a source in a given epoch, and in both adjacent or closely spaced epochs, suggest variability on time-scales shorter than the shortest epoch spacing of 1 d.

ACKNOWLEDGEMENTS

The National Radio Astronomy Observatory is a facility of the National Science Foundation operated under cooperative agreement by Associated Universities, Inc. SAD acknowledges the M2FINDERS project from the European Research Council under the European Union's Horizon 2020 research and innovation programme (Grant No. 101018682). ETO acknowledges support from a Science and Technology Facilities Council PhD studentship (Grant No. ST/X508408/1).

DATA AVAILABILITY

The VLBA data used in this work (BF117, BF123A, BF123B, BF123C, BF131A, BF131B, BF131C, BF131D) are available from

Downloaded from academic.oup.com/mnras/article/552/4/stag1806/8834038 by guest on 23 October 2026

the NRAO data archive (https://data.nrao.edu). The data underlying this article will be shared upon reasonable request to the corresponding author.

REFERENCES

Abt H. A., Wang R., Cardona O., 1991, ApJ, 367, 155
Andre P., 1996, in Taylor A. R., Paredes J. M., eds, ASP Conf. Ser. Vol. 93, Radio Emission from the Stars and the Sun. Astron. Soc. Pac., San Francisco, p. 273
Andre P., Phillips R. B., Lestrade J.-F., Klein K.-L., 1991, ApJ, 376, 630
Balega Y. Y., Chentsov E. L., Leushin V. V., Rzaev A. K., Weigelt G., 2014, Astrophys. Bull., 69, 46
Benz A., 2002, Plasma Astrophysics, 2nd edn. Kluwer, Dordrecht
Benz A. O., Guedel M., 1994, A&A, 285, 621
Bossi M., Gaspani A., Scardia M., Tadini M., 1989, A&A, 222, 117
Bower G. C., Plambeck R. L., Bolatto A., McCrady N., Graham J. R., de Pater I., Liu M. C., Baganoff F. K., 2003, ApJ, 598, 1140
Bridle A. H., Schwab F. R., 1999, in Taylor G. B., Carilli C. L., Perley R. A., eds, ASP Conf. Ser. Vol. 180, Synthesis Imaging in Radio Astronomy II. Astron. Soc. Pac., San Francisco, p. 371
CASA Team, 2022, PASP, 134, 114501
Choi J., Dotter A., Conroy C., Cantiello M., Paxton B., Johnson B. D., 2016, ApJ, 823, 102
Churchwell E., Felli M., Wood D. O. S., Massi M., 1987, ApJ, 321, 516
Condon J., Ransom S., 2016, Essential Radio Astronomy. Princeton Series in Modern Observational Astronomy. Princeton Univ. Press, Princeton
Deane R. P. et al., 2024, MNRAS, 529, 2428
Deller A. T., Tingay S. J., Bailes M., West C., 2007, PASP, 119, 318
Deller A. T. et al., 2011, PASP, 123, 275
Deller A. T., Forbrich J., Loinard L., 2013, A&A, 552, A51
Dotter A., 2016, ApJS, 222, 8
Dulk G. A., 1985, ARA&A, 23, 169
Dzib S. A. et al., 2013, ApJ, 775, 63
Dzib S. A. et al., 2015, ApJ, 801, 91
Dzib S. A., Forbrich J., Reid M. J., Menten K. M., 2021, ApJ, 906, 24
Dzib S. A., Loinard L., Launhardt R., Ordóñez-Toro J., 2024, A&A, 686, A176
Dzib S. A. et al., 2026a, A&A, 708, A299
Dzib S. A. et al., 2026b, A&A, 708, A300
Fang M., Kim J. S., Pascucci I., Apai D., 2021, ApJ, 908, 49
Feigelson E. D., 2010, Proc. Natl. Acad. Sci., 107, 7153
Feigelson E. D., Montmerle T., 1999, ARA&A, 37, 363
Feigelson E. D., Carkner L., Wilking B. A., 1998, ApJ, 494, L215
Feigelson E. D., Garmire G. P., Pravdo S. H., 2002, ApJ, 572, 335
Felli M., Spencer R., 1989, Very Long Baseline Interferometry, Nato Science Series C, ASIC, Vol. 283. Springer, Dordrecht
Forbrich J., Wolk S. J., 2013, A&A, 551, A56
Forbrich J., Menten K. M., Reid M. J., 2008, A&A, 477, 267
Forbrich J. et al., 2016, ApJ, 822, 93
Forbrich J., Reid M. J., Menten K. M., Rivilla V. M., Wolk S. J., Rau U., Chandler C. J., 2017, ApJ, 844, 109
Forbrich J., Dzib S. A., Reid M. J., Menten K. M., 2021, ApJ, 906, 23
Garay G., Moran J. M., Reid M. J., 1987, ApJ, 314, 535
Garrett M. A., Porcas R. W., Pedlar A., Muxlow T. W. B., Garrington S. T., 1999, New Astron. Rev., 43, 519
Getman K. V., Feigelson E. D., 2021, ApJ, 916, 32
Getman K. V. et al., 2005, ApJS, 160, 319
Getman K. V., Feigelson E. D., Garmire G. P., 2021, ApJ, 920, 154
Getman K. V., Feigelson E. D., Garmire G. P., Broos P. S., Kuhn M. A., Preibisch T., Airapetian V. S., 2022, ApJ, 935, 43
GRAVITY Collaboration, 2018, A&A, 620, A116
Greisen E. W., 2003, in Heck A., ed., Astrophysics and Space Science Library Vol. 285, Information Handling in Astronomy – Historical Vistas. p. 109
Großschedl J. E. et al., 2019, A&A, 622, A149
Güdel M., 2002, ARA&A, 40, 217
Güdel M., 2004, A&AR, 12, 71
Guedel M., Benz A. O., 1993, ApJ, 405, L63
Herrera Ruiz N. et al., 2017, A&A, 607, A132
Hillenbrand L. A., 1997, AJ, 113, 1733
Hillenbrand L. A., Hoffer A. S., Herczeg G. J., 2013, AJ, 146, 85
Kaur S. et al., 2024, A&A, 690, A303
Kounkel M. et al., 2014, ApJ, 790, 49
Kounkel M. et al., 2017, ApJ, 834, 142
Kraus S. et al., 2009, A&A, 497, 195
Kuhn M. A., Hillenbrand L. A., Sills A., Feigelson E. D., Getman K. V., 2019, ApJ, 870, 32
Launhardt R., Loinard L., Dzib S. A., Forbrich J., Bower G. C., Henning T. K., Mioduszewski A. J., Reffert S., 2022, ApJ, 931, 43
Levato H., Abt H. A., 1976, PASP, 88, 712
Lohsen E., 1976, Inf. Bull. Var. Stars, 1129, 1
Luhman K. L., 2024, AJ, 168, 230
Megeath S. T. et al., 2012, AJ, 144, 192
Meingast S. et al., 2016, A&A, 587, A153
Menten K. M., Reid M. J., Forbrich J., Brunthaler A., 2007, A&A, 474, 515
Middelberg E. et al., 2013, A&A, 551, A97
Morales-Calderón M. et al., 2012, ApJ, 753, 149
Osten R. A., Wolk S. J., 2009, ApJ, 691, 1128
Petr M. G., Coudé du Foresto V., Beckwith S. V. W., Richichi A., McCaughrean M. J., 1998, ApJ, 500, 825
Prisinzano L. et al., 2008, ApJ, 677, 401
Rau U., Cornwell T. J., 2011, A&A, 532, A71
Reid M. J., Brunthaler A., 2004, ApJ, 616, 872
Ricci L., Robberto M., Soderblom D. R., 2008, AJ, 136, 2136
Rivilla V. M., Chandler C. J., Sanz-Forcada J., Jiménez-Serra I., Forbrich J., Martín-Pintado J., 2015, ApJ, 808, 146
Rodríguez L. F., Loinard L., Zapata L. A., 2024, ApJ, 960, L14
Rybicki G. B., Lightman A. P., 1986, Radiative Processes in Astrophysics. Wiley-VCH
Samus' N. N., Kazarovets E. V., Durlevich O. V., Kireeva N. N., Pastukhova E. N., 2017, Astron. Rep., 61, 80
Scaife A., 2012, Astron. Rev., 7, 26
Schertl D., Balega Y. Y., Preibisch T., Weigelt G., 2003, A&A, 402, 267
Sheehan P. D., Eisner J. A., Mann R. K., Williams J. P., 2016, ApJ, 831, 155
Sicilia-Aguilar A. et al., 2005, AJ, 129, 363
Simón-Díaz S., Herrero A., Esteban C., Najarro F., 2006, A&A, 448, 351
Thompson A., Moran J., Swenson G., 2017, Interferometry and Synthesis in Radio Astronomy, Astronomy and Astrophysics Library. Springer, Cham
Vargas-González J., 2024, PhD thesis, University of Hertfordshire
Vargas-González J., Forbrich J., Dzib S. A., Bally J., 2021, MNRAS, 506, 3169
Vargas-González J., Forbrich J., Rivilla V. M., Menten K. M., Güdel M., Hacar A., 2023, MNRAS, 522, 56
Waterfall C. O. G., Browning P. K., Fuller G. A., Gordovskyy M., 2019, MNRAS, 483, 917
Wei L., Theissen C. A., Konopacky Q. M., Lu J. R., Hsu C.-C., Kim D., 2024, ApJ, 962, 174
Weigelt G., Balega Y., Preibisch T., Schertl D., Schöller M., Zinnecker H., 1999, A&A, 347, L15
Whitmore B. C. et al., 2016, AJ, 151, 134
Wilson T. L., Rohlfs K., Hüttemeister S., 2009, Tools of Radio Astronomy. Springer, Berlin
Windhorst R. A., Fomalont E. B., Partridge R. B., Lowenthal J. D., 1993, ApJ, 405, 498
Wrobel J. M., 1995, in Zensus J. A., Diamond P. J., Napier P. J., eds, ASP Conf. Ser. Vol. 82, Very Long Baseline Interferometry and the VLBA. Astron. Soc. Pac., San Francisco, p. 411
Yanza V. et al., 2022, AJ, 163, 276
Zapata L. A., Rodríguez L. F., Kurtz S. E., O'Dell C. R., 2004a, AJ, 127, 2252

Downloaded from academic.oup.com/mnras/article/552/4/stag1806/8834038 by guest on 23 October 2026

Zapata L. A., Rodríguez L. F., Kurtz S. E., O'Dell C. R., Ho P. T. P., 2004b, ApJ, 610, L121
Zhao B. et al., 2020, Space Sci. Rev., 216, 43

SUPPLEMENTARY MATERIAL

Supplementary material are available at *MNRAS* online.

table2_mrt.txt
table3_mrt.txt

Please note: Oxford University Press is not responsible for the content or functionality of any supporting materials supplied by the authors. Any queries (other than missing material) should be directed to the corresponding author for the article.

APPENDIX A

A1 VLBA sources at large separations

We find a subset of sources at larger separations (>800 mas) from their respective phase centre. These detections are likely to be genuine, but the effective detection threshold increases with distance from the phase centre. We therefore report them separately from our main sample. Fig. A1 shows the oversampled images (see Section 3) of four of these sources that have the highest signal-to-noise. We search for counterparts for these sources using the *Hubble* catalogue of B. C. Whitmore et al. (2016) which is a master catalogue from archival HST imaging with the ACS, WFPC2 and WFC3 instruments, and the VISTA near-infrared survey of the Orion A molecular cloud called VISION of S. Meingast et al. (2016). We use a search radius of 0.5 arcsec as we did in Section 4.2, and find 5 of these sources have counterparts from the *Hubble* catalogue and find no counterparts in the VISION catalogue. The sources that have *Hubble* counterparts are listed in Table A1 with the separation between the VLBA detection and the counterpart. Additionally, Table A2 shows source details for all VLBA sources at larger separations. Here the separation is defined as

Table A1. VLBA sources at larger separations from their respective phase centres that have *Hubble* counterparts and the separations between the VLBA source positions and the *Hubble* counterpart (B. C. Whitmore et al. 2016).

[FRM2016]	$\Delta\theta$ (mas)
ONC042	389.2 ± 0.2
ONC224	101.7 ± 0.3
ONC277	362.3 ± 0.2
ONC349	86.0 ± 0.2
ONC484	63.7 ± 0.2

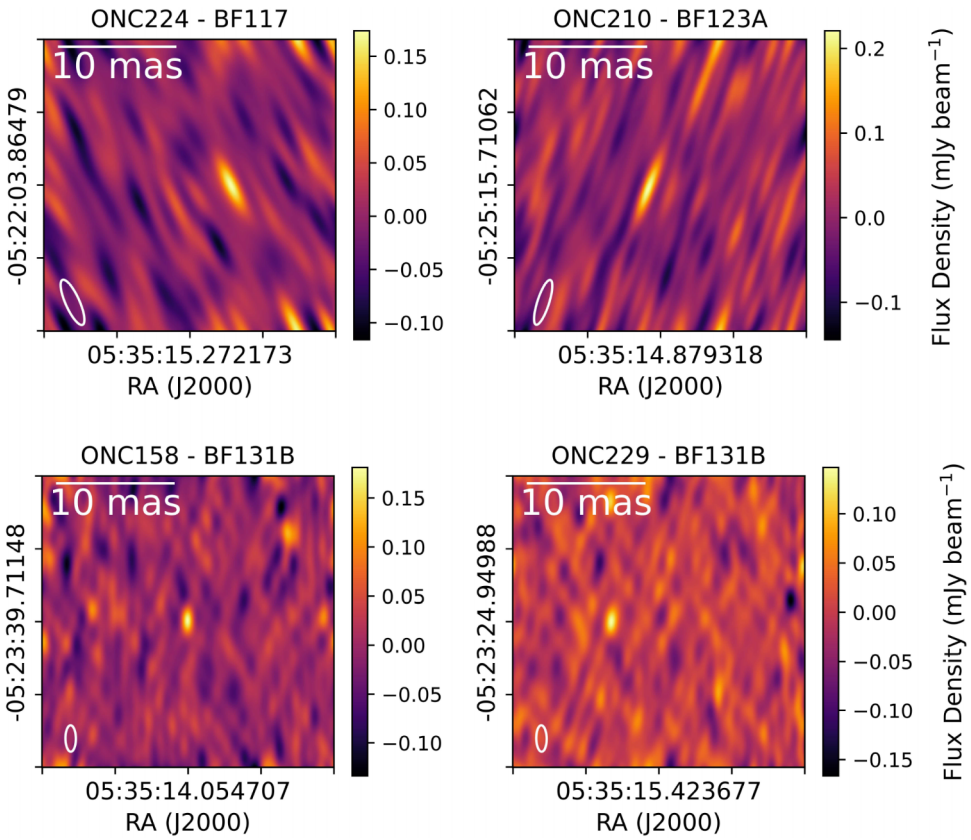


Figure A1. Grid plot showing the images of the four brightest source detection candidates that are at high separations from their respective phase centre. The coordinates of the centre of the image are shown: bottom left is the synthesized beam and upper left is a scale bar showing 10 mas (∼4 AU at the distance of the ONC).

Downloaded from academic.oup.com/mnras/article/552/4/stag1806/8834038 by guest on 23 October 2026

Table A2. Table of sources at large separations (>800 mas) from their respective phase centre.

[FRM2016]	COUP[a]	Flux density (mJy beam^{-1})	S/N	α_{J2000}	σ_α (mas)	δ_{J2000}	σ_δ (mas)	$\Delta\theta^1$ (mas)
BF117:								
ONC223	–	0.24 ± 0.02	10.6	05:35:15.219164	0.160	−05:23:58.59288	0.333	1066.2 ± 6.5
ONC224	–	0.19 ± 0.01	13.6	05:35:15.272173	0.106	−05:22:03.86479	0.213	1365.0 ± 3.8
BF123A:								
ONC210	–	0.37 ± 0.02	15.7	05:35:14.879318	0.109	−05:25:15.71062	0.317	979.7 ± 3.7
BF123C:								
ONC364	–	0.21 ± 0.02	9.8	05:35:17.658061	0.021	−05:23:39.31981	0.116	1565.2 ± 0.3
BF131A:								
ONC029	365	0.15 ± 0.02	9.3	05:35:10.162020	0.046	−05:23:22.48437	0.158	1212.9 ± 0.8
ONC042	–	0.19 ± 0.01	13.2	05:35:10.916948	0.027	−05:23:27.58121	0.127	1016.3 ± 0.3
ONC054	–	0.14 ± 0.02	8.6	05:35:11.512994	0.048	−05:22:55.26907	0.149	1070.4 ± 0.7
ONC077	470	0.16 ± 0.02	8.7	05:35:12.271003	0.083	−05:23:48.93483	0.246	894.9 ± 1.6
ONC532[b]	1296	0.49 ± 0.05	11.5	05:35:24.573942	0.059	−05:19:32.34703	0.151	907.7 ± 0.9
BF131B:								
ONC072	–	0.16 ± 0.01	11.4	05:35:12.119197	0.024	−05:22:13.17631	0.147	1015.5 ± 0.3
ONC120	–	0.19 ± 0.02	11.8	05:35:13.310415	0.019	−05:23:28.71650	0.147	903.7 ± 0.2
ONC158	602	0.23 ± 0.02	13.7	05:35:14.054707	0.014	−05:23:39.71148	0.101	1272.1 ± 0.1
ONC229	–	0.19 ± 0.01	19.5	05:35:15.423677	0.017	−05:23:24.94988	0.069	1025.7 ± 0.1
ONC349	879	0.14 ± 0.01	9.5	05:35:17.390507	0.029	−05:23:05.86332	0.187	996.9 ± 0.4
ONC409	976	0.24 ± 0.03	10.4	05:35:18.480052	0.051	−05:20:43.60629	0.160	962.6 ± 0.7
ONC484	–	0.20 ± 0.02	11.1	05:35:21.070363	0.027	−05:22:26.14951	0.141	956.0 ± 0.3
BF131C:								
ONC240	717	0.31 ± 0.02	11.5	05:35:15.573475	0.037	−05:23:38.08918	0.139	865.0 ± 0.4
BF131D:								
ONC210	–	0.26 ± 0.02	10.8	05:35:14.727479	0.025	−05:25:13.89417	0.182	1583.0 ± 0.5
ONC277	780	0.12 ± 0.01	10.9	05:35:16.134949	0.017	−05:23:24.06439	0.165	1080.8 ± 0.3

Notes. Columns are (left to right): source number from J. Forbrich et al. (2016), COUP number from K. V. Getman et al. (2005), flux density, signal-to-noise, J2000 right ascension and declination, both with uncertainties, total separation from nominal VLA position.
[a]The respective phase centre is associated with a COUP counterpart, as these sources are at high separations. They might not be directly associated with the X-ray counterpart.
[b]Source is outside the ∼80 per cent power point of the FWHM and the uncertainties might be underestimated.

$$\Delta\alpha = (\alpha_{\rm VLBA} - \alpha_{\rm PC}) \cdot \cos\delta \qquad \text{(A1)}$$
$$\Delta\delta = (\delta_{\rm VLBA} - \delta_{\rm PC})$$
$$\Delta\theta = \sqrt{\Delta\alpha^2 + \Delta\delta^2}$$

where $\Delta\alpha$ is the separation in right ascension, $\Delta\delta$ is the separation in declination, and $\Delta\theta$ is the total separation between the VLBA position and the phase centre (denoted by 'PC'). It should be noted that the COUP counterparts listed in Table A2 are associated with the respective phase centre and might not be directly related to the VLBA sources due to their large angular separation.

APPENDIX B

This appendix discusses more details of specific sources that exhibit higher variability with VFs ≥ 5 [e.g. COUP number, mass estimates, spectral types from L. A. Hillenbrand et al. (2013) and/or YSO class from L. Prisinzano et al. (2008) where available].

B0.1 ONC003.1

ONC003.1 is only detected in BF131C with a peak flux density of 0.71 ± 0.08 mJy beam^{-1}. A lower limit for the VF of this source is >6.1 using the 5.5σ value of the lowest rms as an upper limit (see Section 3.1 for discussion of variability factors). Unlike the other higher variable sources (discussed below) ONC003 does not have a COUP counterpart. As detailed in Section 4 this could be due to variability or this source could be a very deeply embedded object that is not detected in X-ray. This source does have a VLBA radio counterpart (ONC003.2 detected in BF131D) with a separation of 0.50 arcsec (see Table 3).

B0.2 ONC016 (COUP 322 or 2MASS J05350873-0522566)

L. A. Hillenbrand et al. (2013) list ONC016 as spectral type M1.5. L. Wei et al. (2024) estimate the mass using the 'MIST' stellar evolutionary model as 0.829 ± 0.064 $M_\odot$ as part of their near-infrared 'NIRSPEC' work using the Keck II 10 m telescope. K. V. Getman & E. D. Feigelson (2021) estimate the mass as 0.5 $M_\odot$ from their *Chandra* study. This source is detected in BF131A, as seen in Table 2, with an averaged peak flux density of 1.56 ± 0.03 mJy beam^{-1} for the whole epoch. As it is a single detection a lower limit of the VF is >12, this can be seen in Fig. B1.

B0.3 ONC066 (COUP 450 or GMR A)

ONC066 is detected in all VLBA epochs as seen in Table 2. It has an averaged peak flux density of 10.27 ± 0.18 mJy beam^{-1} in BF131C and the lowest flux density of 1.16 ± 0.02

Downloaded from academic.oup.com/mnras/article/552/4/stag1806/8834038 by guest on 23 October 2026

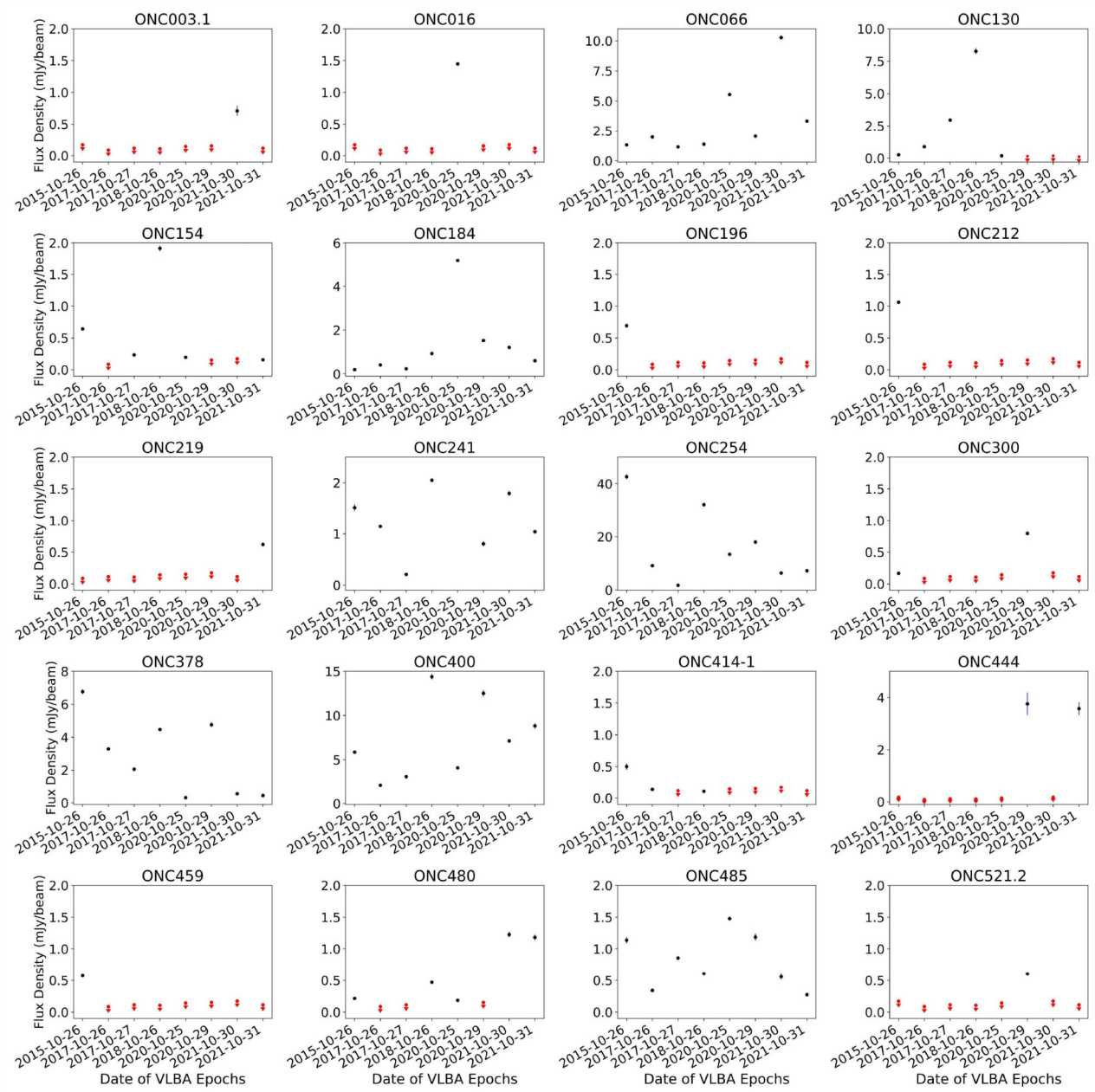


Figure B1. Grid plot of light curves for sources with higher variability factors (≥ 5). This plot shows the primary beam-corrected flux density measurements for the source for each epoch as measured by 'imfit'. The flux density is shown in black, and where a source was not detected the upper limit of the 5.5σ value of the rms is shown in red.

mJy beam^{-1} in BF123B, which corresponds to the highest variability factor of 8.8 $\pm$ 0.2. The increase in flux density in BF131C also results in the variability factor being higher between BF131B and BF131C at VF = 5.0 $\pm$ 0.2 (representing a time-scale of $\sim$1 yr) and between BF131C and BF131D (representing a time-scale of 1 d) at VF = 3.1 $\pm$ 0.1. These higher VFs point to potential variability occurring for ONC066 on shorter time-scales at least in the case of BF131C and the adjacent epochs.

B0.4 ONC154 (COUP 594)

L. A. Zapata et al. (2004b) concluded that this is a counterpart of the X-ray source COUP 594 as part of their VLA survey, and detections of circular polarization ($\sim$20 per cent right-circular polarization) indicate gyrosynchrotron emission associated with a pre-main-sequence star. Table 2 shows the highest averaged peak flux density is 1.91 $\pm$ 0.04 mJy beam^{-1} in BF123C and the lowest flux density of 0.17 $\pm$ 0.02 mJy beam^{-1} in BF131D, which corresponds to VF = 12.0 $\pm$ 1.8.

Downloaded from academic.oup.com/mnras/article/552/4/stag1806/8834038 by guest on 23 October 2026

B0.5 ONC196 (COUP 648)

ONC196 is classified by L. A. Hillenbrand et al. (2013) as spectral type K3-M2, and K. V. Getman & E. D. Feigelson (2021) estimate the mass as 2.5 $M_\odot$ from their *Chandra* study. It is detected in BF117 epoch and has a peak flux density of 0.69 ± 0.03 mJy beam^{-1}. As this source is only detected once a lower limit of the variability factor was estimated as >6.0.

B0.6 ONC212 (COUP 670)

ONC212 is classified as spectral type K3-M2 by L. A. Hillenbrand et al. (2013). The mass is listed as 0.434 ± 0.032 $M_\odot$ by L. Wei et al. (2024) from their 'MIST' model using near-infrared 'NIRSPEC' data from the Keck II 10 m telescope. The peak flux density is 1.06 ± 0.02 mJy beam^{-1}. This source is only detected in BF117 epoch; therefore, the lower limit of the VF is >9.2.

B0.7 ONC219 (COUP 680)

ONC219 is only detected in BF131D epoch, with a peak flux density of 0.62 ± 0.03 mJy beam^{-1}, so a lower limit of the VF was calculated as >5.3. This source is also discussed by J. Vargas-González et al. (2023) as a millimetre flare source observed with the Atacama Large Millimetre/submillimetre Array, there are 9 other sources discussed by J. Vargas-González et al. (2023) that have centimetre and millimetre counterparts.

B0.8 ONC241 (COUP 718 or V1501 Ori)

M. Morales-Calderón et al. (2012) classified ONC241 as an accreting T-Tauri star and possible eclipsing binary as part of their Spitzer Exploration Science Program YSOVAR, and A. Sicilia-Aguilar et al. (2005) concluded it is likely a weak-lined T-Tauri star from their 6.5 m MMT data. Additionally, L. A. Hillenbrand et al. (2013) give a spectral classification of K4-M1. L. Wei et al. (2024) estimate the mass using the 'MIST' (J. Choi et al. 2016; A. Dotter 2016) stellar evolutionary model as 0.892 ± 0.063 $M_\odot$ using near-infrared 'NIRSPEC' data from the Keck II 10 m telescope. Fig. B1 and Table 2 show the highest peak averaged flux density is 2.99 ± 0.07 mJy beam^{-1} in BF131A and the lowest is 0.22 ± 0.02 in the BF123B epoch which corresponds to VF = 13.5 ± 1.2 on a time-scale of 1 yr.

B0.9 ONC300.2 (COUP 801)

ONC300.2 is classified as spectral type K4-K7 by L. A. Hillenbrand et al. (2013). The mass is listed as 0.437 ± 0.031 $M_\odot$ by L. Wei et al. (2024) from the 'MIST' model (J. Choi et al. 2016; A. Dotter 2016). The peak flux density is 0.97 ± 0.04 mJy beam^{-1} in BF131B, resulting in a lower limit of >8.2 for the VF. This source has a VLBA radio counterpart (ONC300.1 detected in BF117) with a separation of 0.57 arcsec (see Table 3).

B0.10 ONC400 (COUP 965 or V1229 Ori)

ONC400 is classified in the General Catalogue of Variable Stars (GCVS) as an irregular eruptive variable of type'IN' or Orion variable (N. N. Samus' et al. 2017) and as spectral type G8-M2 by L. A. Hillenbrand et al. (2013). G. Garay et al. (1987) discuss this source as a T-Tauri star that exhibits radio variability from their VLA observations at 1.5, 4.9, 15.0, and 22.5 GHz and P. D. Sheehan et al. (2016) observed this with the VLA as a radio variable star at 3.6 cm (8 GHz). The mass was estimated by L. Wei et al. (2024) as 0.487 ± 0.063 $M_\odot$ using the 'MIST' stellar model (J. Choi et al. 2016; A. Dotter 2016) using near-infrared 'NIRSPEC' data from the Keck II 10 m telescope. ONC400 has a peak-averaged flux density of 14.38 ± 0.32 mJy beam^{-1} in BF123C and lowest of 2.10 ± 0.06 in BF123A which corresponds to VF = 6.8 ± 0.3 on a time-scale of 1 yr.

B0.11 ONC414.1 (COUP 985 or MV Ori)

ONC414.1 is classified as spectral type F8-K4 by (L. A. Hillenbrand et al. 2013). It is a radio variable source as discussed by J. Forbrich et al. (2017). Table 2 shows it has a peak-averaged flux density of 0.69 ± 0.07 mJy beam^{-1} in BF117, and a lowest flux density of 0.15 ± 0.01 mJy beam^{-1} in BF123C which results in VF = 4.5 ± 0.6. This source has a counterpart (ONC414.2), also discussed by S. A. Dzib et al. (2021), detected in epochs BF123B and BF123C at a separation of 0.22 arcsec (see Table 3).

B0.12 ONC444 (COUP 1035)

ONC444.1 and ONC444.2 are two separate sources detected in BF131B and BF131D as seen in Table 3 where the separation from the nominal VLA position is: 502.08 ± 1.30 and 133.98 ± 0.18, respectively. Considering the time-scale between the detections of only a year and the large separation these are likely two separate sources. S. T. Megeath et al. (2012) classify ONC444.2 as a YSO with a disc using mid-infrared data from *Spitzer*. Their peak flux densities are: ONC444.1 = 3.76 ± 0.43 mJy beam^{-1} resulting in a lower limit of >32.4 for the VF and ONC444.2 = 3.57 ± 0.25 mJy beam^{-1} which gives a lower limit of >30.8 for the VF. It should be noted these sources sit outside the ∼80 per cent power point of the FWHM where they are both ∼ 5.5 arcmin from the pointing centre so the uncertainties could be underestimated, these are flagged in Tables 2 and 3 to show this.

B0.13 ONC459 (COUP 1083 or V∗ V1517 Ori)

ONC459 is classified as a class III YSO by L. Prisinzano et al. (2008) and L. A. Hillenbrand et al. (2013) classify it as spectral type <M0. It is only detected in BF117 epoch with a flux density of 0.65 ± 0.02 mJy beam^{-1}. Therefore, a lower limit of the VF was calculated as >4.9 using the 5.5σ value of the lowest rms value which can be seen in Fig. B1.

B0.14 ONC480 (COUP 1116 or V1230 Ori)

ONC480 is classified as spectral type B by L. A. Hillenbrand et al. (2013). P. D. Sheehan et al. (2016) found that this is a variable source at 1.3 cm (23 GHz) from their VLA observations. The peak-averaged flux density is 1.23 ± 0.04 in BF131C and lowest of 0.19 ± 0.02 in BF131A, which results in VF = 6.5 ± 0.4 across a timespan of 1 yr. S. A. Dzib et al. (2026b) discuss this source and conclude from their astrometry that it is likely a binary system with a low-mass YSO companion. They suggested that the primary star, of spectral type B1, is the source detected by *Gaia*,

Downloaded from academic.oup.com/mnras/article/552/4/stag1806/8834038 by guest on 23 October 2026

while the companion is likely a lower-mass star responsible for the non-thermal emission detected here.

B0.15 ONC485 (COUP 1130 or V1399 Ori)

ONC485 is classified as spectral type G8-K5 by L. Prisinzano et al. (2008). L. Wei et al. (2024) estimate the mass using the 'MIST' stellar evolutionary model as $0.446 \pm 0.027\,M_{\odot}$ from their near-infrared 'NIRSPEC' work from Keck II 10 m telescope observations. The peak-averaged flux density is 1.48 ± 0.03 mJy beam^{-1} in BF131A and the lowest is 0.27 ± 0.02 mJy beam^{-1} in BF131D. This corresponds to VF $= 5.5 \pm 0.5$ across a timespan of 1 yr.

B0.16 ONC521.2 (COUP 1261 or V∗ V1342)

ONC521.2 is detected in BF131B at a peak flux density of 0.60 ± 0.02 mJy beam^{-1}. It is spectral type M3-M3.5e (L. A. Hillenbrand et al. 2013) and has a lower limit of >5.2 for the VF. This source has a VLBA counterpart detected in epoch BF117 at a separation of 0.31 (see Table 3). This source is outside the ∼80 per cent power point of the FWHM at a separation of ~ 3.3 arcmin from the pointing centre. This source is flagged in Tables 2 and 3 as having potentially underestimated uncertainties.

This paper has been typeset from a TEX/LATEX file prepared by the author.

Downloaded from academic.oup.com/mnras/article/552/4/stag1806/8834038 by guest on 23 October 2026

© The Author(s) 2026.
Published by Oxford University Press on behalf of Royal Astronomical Society. This is an Open Access article distributed under the terms of the Creative Commons Attribution License (https://creativecommons.org/licenses/by/4.0/), which permits unrestricted reuse, distribution, and reproduction in any medium, provided the original work is properly cited.